Department of Physics and Astronomy

University of Heidelberg

Bachelor Thesis in Physics

submitted by

Felix Clas Borchers

born in Bonn-Duisdorf, Germany

July 2023

Modelling of Absorption Imaging of degenerate Fermi Gases in ultracold Atom Experiments

This Bachelor Thesis has been carried out
by Felix Borchers at the
Physikalisches Institut of the University of Heidelberg
under the supervision of
Prof. Dr. Lauriane Chomaz

Abstract

Absorption imaging techniques are an essential tool in the study of ultracold atomic gases. In our experiment both bosonic and fermionic atomic clouds are studied using this method. For highly degenerate Fermi gases at low temperatures the reliable extraction of fitted cloud parameters is particularly challenging. In this thesis we construct a numerical simulation of the imaging process and the noise sources involved. This allows us to compare input cloud parameters to parameters extracted from the simulated images and determine their accuracy and the involved uncertainties.

We show that the degeneracy parameter T/T_F is accurately resolved at sufficiently high cloud densities and light intensities if $T/T_\mathrm{F} < 0.5$. We additionally find that the atom number is reliably estimated, even in low density regimes. In the case of time-of-flight measurements we find that for low T/T_F it is necessary to fit the Fermi density distribution, because the temperature is systematically overestimated by the fit of the Gaussian density distribution. We compare the uncertainty in T/T_F as directly calculated from the cloud parameters to the determination from atom number and temperature, and show that they provide a similar accuracy. Furthermore, we determine that by employing a principal component analysis to distinguish correlated noise associated with the underlying experimental parameters and uncorrelated noise from the imaging procedure the fit accuracy can be significantly improved.

Zusammenfassung

Absorptionsabbildungstechniken sind ein wesentliches Instrument für die Untersuchung ultrakalter Atomgase. In unserem Experiment werden sowohl bosonische als auch fermionische Atomwolken mit dieser Methode untersucht. Für hochgradig entartete Fermi-Gase bei tiefen Temperaturen stellt die Extraktion der Atomwolkenparameter eine besondere Herausforderung dar. In dieser Arbeit erstellen wir eine numerische Simulation des Abbildungsprozesses und der beteiligten Rauschquellen. Dadurch können wir die eingegebenen Atomwolkenparameter mit den aus den simulierten Bildern extrahierten Parametern vergleichen und deren Genauigkeit sowie die damit verbundenen Unsicherheiten bestimmen.

Wir zeigen, dass der Entartungsparameter T/T_F bei ausreichend hohen Dichten und Lichtintensitäten im Bereich $T/T_\mathrm{F} < 0.5$ genau aufgelöst wird. Wir finden außerdem, dass die Anzahl der Atome auch bei niedrigen Dichten zuverlässig geschätzt wird. Bei Flugzeitmessungen stellen wir fest, dass es für niedrige T/T_F notwendig ist, die Parameter mit Hilfe der Fermi-Dichteverteilung zu bestimmen, da die Bestimmung durch die Gausssche-Dichteverteilung die Temperatur systematisch überschätzt. Wir vergleichen die Unsicherheit in T/T_F, die direkt aus den Atomwolkenparametern bestimmt wird, mit der Bestimmung aus Atomzahl und Temperatur und zeigen, dass sie ähnlich genau sind. Darüber hinaus stellen wir fest, dass durch die Anwendung einer Hauptkomponentenanalyse zur Unterscheidung von korreliertem Rauschen, das mit den zugrundeliegenden experimentellen Parametern verbunden ist, und unkorreliertem Rauschen aus dem Abbildungsverfahren die Parameterbestimmung erheblich verbessert werden kann.

Contents

1 Introduction

The study of ultracold-atomic quantum gases provides a highly controllable setting to study quantum many-body physics. In particular the ability to arbitrarily tune the effective interaction strength of different particles by means of Feshbach resonances allows studying a wide variety of phenomena [Chin et al., 2010]. Among them is the observation of emergent quasi-particles such as the polaron. The polaron describes the quasi-particle character of a single particle impurity with a many-body background. In the setting of ultracold gases, the Fermi polaron constitutes the interaction of an impurity in a bath obeying Fermi statistics.

Since the first realization of an attractive Fermi polaron with ^{6}Li atoms in 2009 [Schirotzek et al., 2009], a wide variety of Fermi polarons have been studied experimentally [Scazza et al., 2022, Massignan et al., 2014]. One still largely unexplored regime remains for systems of large mass imbalance, such as ^{133}Cs immersed in a quantum-degenerate Fermi sea of ^{6}Li with a mass ratio of ~ 22. This limit is interesting due to its relevance in the physics close to the orthogonality catastrophe [Schmidt et al., 2018], as well as observed resonances in the impurity-impurity scattering length [Tran et al., 2021, Enss et al., 2020]. To measure this physics it is necessary to be able to resolve low numbers of atoms and their temperature with a high signal-to-noise ratio.

A central characteristic of ultracold Fermi gases is provided by the temperature parameter T/T_F. In the case of large mass imbalances the polaron ground state energy and bandwidth are highly dependent on this parameter [Hu and Liu, 2022], necessitating a precise estimate. Furthermore, the parameter plays a central role in approaching the so-called orthogonality catastrophe in the zero-temperature limit [Schmidt et al., 2018]. There exist multiple methods to determining the parameter T/T_F, with the measurement of the temperature from the Bose particle time-of-flight being the most common. The measurement is usually preferred due to the reliability of cloud parameter estimations from Gaussian density profiles. In our experiment a Fermi polaron is created by overlapping a thermal gas of ^{133}Cs with a degenerate single-component Fermi gas of ^{6}Li. Because the optical trap of the Lithium set to the tune-out wavelength of Caesium at 880.217 90 nm [Ratkata et al., 2021], losses are incurred. These losses impede the thermalization process between the two clouds, such that a temperature measurement from the boson cloud becomes unfeasible [Welz, 2024]. An alternative temperature and T/T_F measurement is provided by instead directly imaging the fermionic ^{6}Li cloud. The reliability of this measurement is less understood in the context of our experiment.

In this thesis we will investigate the reliability of estimating cloud parameters of cold Fermi gases by absorption imaging. We build up a numerical model to simulate the absorption and imaging process. In this we take into account various sources of noise and inhomogeneities associated with the camera CCD sensor and imaging laser. We begin with an overview of the physics of cold Fermi gases in Chapter 2. Following this we discuss properties of the imaging light in Chapter 3 and noise sources relevant in the camera description in Chapter 4. In Chapter 5 we expand on the implementation details, as well as choice of parameter space covered by our analysis. We additionally discuss fitting routines and noise reduction tools employed in the extraction of the cloud information from the simulated images. Our results are presented in Chapter 6 before concluding in Chapter 7.

2 Properties of Ideal Boltzmann and Fermi Gases

The central system of interest in the experiment are cold atomic clouds. In our case cold ^{6}Li clouds. The following two sections summarize their dynamics based on the extensive treatment found in [Ketterle and Zwierlein, 2008].

2.1 In-Situ Density Profile

The atomic cloud we want to image by the absorption process consists of ^{6}Li. This atom is a fermion. For the purposes of our analysis we will assume the ^{6}Li atoms to not interact with each other. The quantum statistics of the gas is then given by the Fermi distribution. Given a single-particle Hamiltonian $H = \frac{p^2}{2m} + V(\mathbf{r})$ with potential $V(\mathbf{r})$ and energy eigenvalues E_i, as well as chemical potential μ, the occupation number of atoms in the ith energy eigenstate then can be expressed by

$$\langle n_i \rangle = \frac{1}{\mathrm{e}^{\beta(E_i-\mu)}+1}. \tag{1}$$

If the thermal energy $k_\mathrm{B}T = 1/\beta$ is significantly larger than the spacing of the energy levels ΔE_i the continuum approximation may be used. In this case the energy eigenvalues are replaced by the local classical energy, which yields the corresponding phase-space density. [1]

The number of atoms in a phase-space cell centered at $(\mathbf{r}, \mathbf{p})$ of volume h^3 is

$$f_\mathrm{PSD}(\mathbf{r}, \mathbf{p}) = \frac{1}{\mathrm{e}^{\beta\left(\frac{\mathbf{p}^2}{2m}+V(\mathbf{r})-\mu\right)}+1}. \tag{2}$$

Integrating the momentum dependence yields the number density

$$n(\mathbf{r}) = \int \frac{d^3\mathbf{p}}{(2\pi\hbar)^3} f_\mathrm{PSD}(\mathbf{r}, \mathbf{p}) \tag{3}$$

$$= \frac{1}{\lambda_\mathrm{dB}^3} \mathrm{Li}_{3/2}(-\exp\left[\beta(\mu - V(\mathbf{r}))\right]) \tag{4}$$

with the de Broglie wavelength $\lambda_\mathrm{dB} = \sqrt{\frac{2\pi\hbar}{m k_\mathrm{B} T}}$ and $\mathrm{Li}_{3/2}$ the polylogarithm of order 3/2. In general the polylogarithm of order s is defined by

$$\mathrm{Li}_s(z) = \frac{1}{\Gamma(s)} \int_0^\infty \mathrm{d}t \frac{t^{s-1}}{\mathrm{e}^t/z - 1} \tag{5}$$

for all $z \in \mathbb{C}$.

We obtain the atom number by another integration over all spatial components:

[1] In the experiment the trapping potential is approximately harmonic, i.e. $\Delta E_i = \hbar\omega$, with an angular trapping frequency of $\omega_\mathrm{rad} = 2\pi\,1878\,\mathrm{Hz}$ in the short and $\omega_\mathrm{ax} = 2\pi\,32\,\mathrm{Hz}$ in the long direction. The temperature is about $T = 250\,\mathrm{nK}$. This results in a ratio between thermal energy and energy level spacing of ≈ 2.8 and ≈ 162 for the short and long direction, respectively. Therefore, the continuum approximation is applicable.

$$N = \int d^3\mathbf{r}\, n(\mathbf{r}) = \left(\frac{k_\mathrm{B}T}{\hbar\bar{\omega}}\right) \mathrm{Li}_3(-e^{\beta\mu}) \tag{6}$$

In our case we specify the potential to be harmonic. [2]

$$V(\mathbf{r}) = \frac{1}{2}m\left(\omega_x^2 x^2 + \omega_y^2 y^2 + \omega_z^2 z^2\right) \tag{7}$$

where the ω_i represent the angular trapping frequencies of an optical trap.

We now consider the limiting cases of high and zero temperature of the phase space density. In the high temperature regime the distribution becomes Gaussian, approximating a classical (Boltzmann) gas:

$$n(\mathbf{r}) = \frac{N}{(2\pi)^{3/2}\sigma_x\sigma_y\sigma_z} \exp\left(-\sum_i \frac{x_i^2}{2\sigma_i^2}\right) \tag{8}$$

with the Gaussian size $\sigma_i = \sqrt{\frac{k_\mathrm{B}T}{m\omega_i^2}}$.

In the zero temperature limit, due to the Pauli exclusion principle, all the lowest N states, up to a certain energy, are occupied. This energy is called the Fermi energy $E_F = \mu(T=0)$. The density is then expressed as

$$n_F(\mathbf{r}) = \frac{1}{6\pi^2}\left(\frac{2m}{\hbar^2}\right)^{3/2} (\mu - V(\mathbf{r}))^{3/2} \tag{9}$$

$$= \frac{8}{\pi^2}\frac{N}{R_{Fx}R_{Fy}R_{Fz}}\left[\max\left(1 - \sum_i \frac{x_i^2}{R_{Fi}^2}, 0\right)\right]^{3/2} \tag{10}$$

where $R_{Fi} = \sqrt{\frac{2E_F}{m\omega_i^2}}$.

The density then allows to calculate the relationship between atom number and Fermi energy.

$$N = \int d^3\mathbf{r}\, n_F(\mathbf{r}) = \frac{1}{6}\left(\frac{E_F}{\hbar\bar{\omega}}\right)^3 \tag{11}$$

$$\Leftrightarrow E_F = \hbar\bar{\omega}(6N)^{1/3} \tag{12}$$

The Fermi energy provides a temperature scale T_F defined by $E_F = k_\mathrm{B}T_F$. The high temperature regime is then defined by $T \gg T_F$. At temperatures $T \lesssim T_F$, the low temperature regime, the density profile at the centre of the cloud is rather flat (cf. Eq. (10)). Variations in temperature hence only affects the wings. The most dense parts of the cloud do not contain much information about the cloud's temperature.

As the cloud size changes from the Gaussian radius towards the Fermi radius we want to characterize the size of the cloud in between. This can be done by defining the size

[2] The optical dipole-trap used in the experiment has technically a Gaussian potential shape, which is approximately harmonic at the centre of the trap.

$$R_i^2 = \frac{k_\mathrm{B}T}{m\omega_i^2} f(e^{\mu\beta}) \to \begin{cases} \sigma_i^2, & T/T_\mathrm{F} \gg 1 \\ R_{Fi}^2/2, & T/T_\mathrm{F} \ll 1 \end{cases} \tag{13}$$

with

$$f(x) = \frac{\mathrm{Li}_1(-x)}{\mathrm{Li}_0(-x)} = \frac{1+x}{x}\ln(1+x) \tag{14}$$

Note that in our treatment σ_i and R_i are rescaled by a factor $1/\sqrt{2}$ compared to [Ketterle and Zwierlein, 2008]. This is done in order for σ_i to represent the standard Gaussian cloud size and R_i to represent the Gaussian cloud size in the high temperature limit.

2.2 Column Densities

Above we derived the number density of the gas in three dimensions. In the case of absorption imaging, however, we are more interested in the column density. The column density is obtained by integrating along the beam-camera axis. In the simplest case the axis is along one of the eigen-axis, which we choose to be the z-axis. The rotated case will be discussed later.

By employing the identity

$$\int_{-\infty}^{\infty} dx\ \mathrm{Li}_s\left(ze^{-x^2}\right) = \sqrt{\pi}\mathrm{Li}_{s+\frac{1}{2}}(z) \tag{15}$$

the column density can be obtained as

$$n_\mathrm{2D}(x,y) = n_\mathrm{2D,0}\frac{\mathrm{Li}_2\left(-\exp\left[\beta\mu - \frac{1}{2}\beta m(\omega_x^2x^2+\omega_y^2y^2)\right]\right)}{\mathrm{Li}_2\left(-e^{\mu\beta}\right)} \tag{16}$$

with the peak density $n_\mathrm{2D}(x=0,y=0) = n_\mathrm{2D,0}$.

$$n_\mathrm{2D0} = \frac{N}{2\pi R_xR_y}\frac{\mathrm{Li}_3(-\mathrm{e}^q)}{\mathrm{Li}_2(-\mathrm{e}^q)}f(\mathrm{e}^q) \tag{17}$$

We express the column density by considering (Eq. (13)) as

$$n_{2D} = n_{2D,0}\frac{\mathrm{Li}_2\left(-\exp\left[q - \left(\frac{x^2}{2R_x^2}+\frac{y^2}{2R_y^2}\right)f(e^q)\right]\right)}{\mathrm{Li}_2(-e^q)} \tag{18}$$

where $q = \beta\mu$ is the logarithmic fugacity. It is related to T/T_F by the relation

$$\frac{T}{T_F} = [-6\mathrm{Li}_3(-e^q)]^{-1/3} \tag{19}$$

which can be derived by comparing Eq. (6) and Eq. (12). The relationship in the region $T/T_\mathrm{F} \in [0.1, 1]$ is shown in Figure 1.

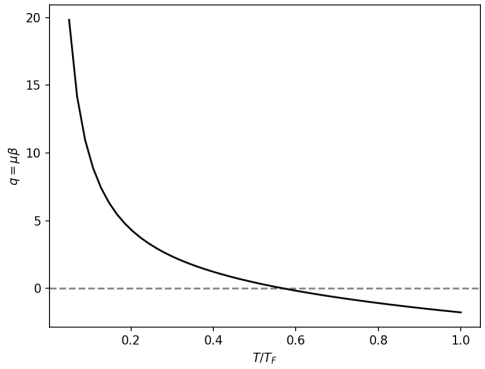

Figure 1: Relationship between the T/T_F parameter and the logarithmic fugacity q.

In the case that the camera is not parallel to any of the semi-axes, due to the ellipsoid shape of the potential the functional form of the column density retains an elliptic symmetry, but with different semi-axes.

In the case of a rotation of the beam-camera axis by an angle θ in the mathematical positive direction in the x-z plane the effective cloud size for the two-dimensional density changes

$$R_x^2 \to R_{x'}^2 = R_x^2 \cos^2(\theta) + R_y^2 \sin^2(\theta), \quad R_y^2 \to R_{y'}^2 = R_{y'}^2 \tag{20}$$

By the definition of the cloud size $R_i = \sqrt{\frac{k_\mathrm{B}T}{m\omega_i^2} f(\mathrm{e}^q)}$ we can associate an effective trapping frequency to the transformed x' axis.

$$\omega_{x'}^2 = \frac{\omega_x^2 \omega_z^2}{\omega_x^2 \sin^2(\theta) + \omega_z^2 \cos^2(\theta)} \tag{21}$$

2.3 Ballistic Expansion

Often, not only the in-situ density is interesting. We are also interested in the expansion of the gas after the harmonic trap is turned off. We only consider the case of the free ballistic expansion. For the free ballistic expansion to hold, the atoms need to be non-interacting, or at least to have a mean free path significantly exceeding the size of the cloud. Then the evolution of an atom initially at point $\mathbf{r}_0$ with momentum $\mathbf{p}_0$ is given by:

$$\mathbf{r}(t) = \mathbf{r}_0 + \frac{\mathbf{p}_0}{m} t \tag{22}$$

$$\mathbf{p}(t) = \mathbf{p}_0 \tag{23}$$

Hence the density at $\mathbf{r}$ can be described by considering the phase space density of all atoms with momentum and position at $t = 0$ such that they reach $\mathbf{r}$ at $t > 0$.

$$n(\mathbf{r},t) = \int d^3\mathbf{r}_0 \int \frac{d^3\mathbf{p}_0}{(2\pi\hbar)^3} f_{\mathrm{PSD}}(\mathbf{r}_0,\mathbf{p}_0)\delta(\mathbf{r}-\mathbf{r}_0-\frac{\mathbf{p}_0}{m}t) \tag{24}$$

$$= -\frac{1}{\lambda_{\mathrm{dB}}}\prod_i \frac{1}{\sqrt{1+\omega_i^2 t^2}} \mathrm{Li}_{3/2}\left[-\exp\left(\beta\mu - \beta\sum_i \frac{1}{2}m\frac{\omega_i^2 x_i^2}{1+\omega_i^2 t^2}\right)\right] \tag{25}$$

This can be seen to just be the in-situ density rescaled by $b_i(t) = \sqrt{1+\omega_i^2 t^2}$.

$$n(\mathbf{r},t) = \frac{1}{b_x(t)b_y(t)b_z(t)} n\left(\frac{x}{b_x(t)}, \frac{y}{b_y(t)}, \frac{z}{b_z(t)}, t=0\right) \tag{26}$$

Equally the size of the cloud is simply rescaled by

$$R_i(t) = b_i(t)R_i(t=0). \tag{27}$$

Indeed, from Eq. (25) we can see that the density after expanding for long times $t \gg \omega_i$ becomes independent of the trap shape

$$\beta\frac{1}{2}m\frac{\omega_i^2 x_i^2}{1+\omega_i^2 t^2} \to \beta\frac{1}{2}m\frac{x_i^2}{t^2}. \tag{28}$$

.

This results holds for generic cloud shapes and hence the shape at long times is insensitive to deviations from the ideal harmonic potential. Hence, the temperature can be measured without relying on precise knowledge of the trapping potential.

Indeed, when the camera-beam axis is rotated with respect to the cloud semi-axes, the expansion can be characterised by the effective trapping frequency along the axis (Equation (21)), i.e.

$$b_{x'}^2 = 1 + \omega_{x'}^2 t^2. \tag{29}$$

3 Absorption Imaging

To measure the density profile of atomic clouds a common technique is *absorption imaging*. The technique consists of placing the atomic cloud between a light source and a detector. The difference between two images with and without the atomic cloud present can then be used to extract information about the density profile of the cloud. In the following we will derive the necessary concepts to connect the measurement technique to the interaction between photons and atoms.

3.1 Atom-Photon Interaction

In general the interaction of atoms and photons works by the absorption and re-emission of the photons by the atoms. If this absorption and re-emission process involves multiple energy levels of the atom and non polarized light the calculation of the interaction become quite involved. In our imaging set-up we use the D_2-line transition at resonance $\lambda = 671\,\mathrm{nm}$. In the regime of high magnetic fields with the light polarized along the polarization axis (defined by the magnetic field direction) the cross-section is given by

$$\sigma_0 = \frac{3\lambda^2}{2\pi}. \tag{30}$$

In the case that the light is polarized perpendicular to the polarization axis only a fourth of the light will interact, which reduces the cross-section to

$$\sigma_0 = \frac{3\lambda^2}{8\pi} \tag{31}$$

as discussed in [Heck, 2012].

The saturation intensity for this transition, i.e. the intensity at which more than a fourth of all atoms is excited simultaneously, is $I_{\text{sat}} = 25.4\,\text{W/m}^2$ [Gehm, 2003] for light polarized along polarization axis. For light polarized perpendicular to the polarization axis the saturation intensity is four times as large $I_{\text{sat}} = 100.8\,\text{W/m}^2$, as the saturation intensity is anti-proportional to the cross-section [Foot, 2005].

If the intensity of the beam incident on the atomic cloud is significantly lower than I_{sat} and the inter-atomic distance is large compared to the mean free path of a photon, the absorption process along the beam-camera axis can be modelled by the Beer-Lambert Law

$$I(x,y) = I_0(x,y)e^{-\sigma_0(\lambda)n(x,y)} \tag{32}$$

where σ_0 is the cross-section for the light-atom interaction and $n(x,y)$ the column density along the beam-camera axis. In our case this density is given by Equation (18). For the Andor and Ximea camera we will consider the cross-section in (30) and (31), respectively.

To obtain the density we require one image of the light intensity after absorption by the cloud, called the absorption Image I_{abs} and another image of the light intensity without the cloud, called the division image I_{div}. To remove offset counts from the image a third image with the imaging light turned off, the dark image I_{dark} is subtracted.

By means of the three pictures we can then calculate the transmission at position (x,y), where the position is given in the object plane of the cloud.

$$T(x,y) = \frac{I_{\text{abs}(x,y)} - I_{\text{dark}}(x,y)}{I_{\text{div}}(x,y) - I_{\text{dark}}(x,y)} = \mathrm{e}^{-\sigma_0 n_{\text{2D}}(x,y)} \tag{33}$$

which is then related to the optical density OD and density by

$$OD(x,y) = n_{\text{2D}}(x,y)\sigma_0 = -\ln\left(T(x,y)\right) \tag{34}$$

Note that the imaging laser intensity profile has a Gaussian shape and is not constant across the image. While the beam is approximately constant in the region of interest, the intensity in the transmission T is only compared locally. Disregarding noise this should not affect the image creation. The effect of features on the intensity profile (e.g. fringes) will be investigated in later chapters.

3.2 Photon Streams

A monochromatic light source with intensity I has an associated mean photon flux $\phi = I/h\nu$ where ν is the light's frequency. The field associated with the light source consists of different modes. Each occupied by a different number of photons. The occupation of these modes follow a probability distribution which is characteristic for a given light source. In the case of a laser the population of the modes can be described by a coherent state. The measurement of the number of photons is then distributed as a counting statistic with mean $\bar{N}$ [Saleh and Teich, 2013]. The mean number of photons $\bar{N}$ collected in an area A during a time interval t is given by:

$$\bar{N} = \frac{IAt}{h\nu} \tag{35}$$

3.3 Light Intensity Profile

As discussed before, it is a central assumption of the Beer-Lambert law, that the light intensity is significantly lower than I_{sat}. We can check the intensity by considering images of the light source taken by the cameras in the setup, these will be referred to as reference images. To analyse the light sources we considered 116 and 96 reference images for the Andor and Ximea camera respectively. The image series had light at a pulse length of $8.4\,\mu$s for the Andor and $3\,\mu$s for the Ximea. Before analysing the images we first subtract a dark image. From the digital images we then obtain the number of photons N_γ incident on a single pixel during the exposure time (cf. Chapter 4). Knowledge of the pulse length t_{pulse}, the imaging wavelength λ and the effective pixel area $A_{\mathrm{px,eff}}$ allows us to calculate the mean intensity incident on pixel (i, j) (similar to Equation (35):

$$\bar{I}(i,j) = \frac{N_\gamma(i,j)E_\lambda}{t_{\mathrm{pulse}}A_{\mathrm{px,eff}}} \tag{36}$$

where $E_\lambda = hc/\lambda$ is the energy of a photon. The effective area of the pixel is only modified by the magnification of the imaging system. The effective pixel area for the Andor is $1.86\,\mu\mathrm{m} \times 1.86\,\mu\mathrm{m}$ instead of the real pixel size $13\,\mu\mathrm{m} \times 13\,\mu\mathrm{m}$. In the case of the Ximea the effective size is $8.28\,\mu\mathrm{m} \times 8.28\,\mu\mathrm{m}$ instead of $4.54\,\mu\mathrm{m} \times 4.54\,\mu\mathrm{m}$. The calculated mean and variance for the intensity and photon number across the image series are displayed in Figure 2.

The mean intensity we calculated for the Andor, $I = 0.21\,\mathrm{I_{sat}} = 5.3\,\mathrm{W/m^2}$ agrees with the light intensity set by the experimental control. For the Ximea on the other hand the light intensity turned out far lower than expected $I = 0.0068 I_{\mathrm{sat}} = 0.7\,\mathrm{W/m^2}$. Furthermore, in both mean images fringes and intensity gradients are visible. Later we want to consider the influence of these spatial inhomogeneities on the fit accuracy, wherefore we extract the mean intensity in the region we expect the atomic cloud to be visible. These regions are shown in Figure 3. The mean intensity in the region of interest is $0.18 I_{\mathrm{sat}}$ for the Andor and $0.005 I_{\mathrm{sat}}$ for the Ximea.

If the variation in counts between images would be dominated by shot noise we expect a ratio of the variance and mean close to unity. In the case of the Andor the ratio, however, is 4.4, whereas in the case of the Ximea is 1.7. This suggests that there are other sources of noise besides the photon shot noise, which we discuss in the following chapter.

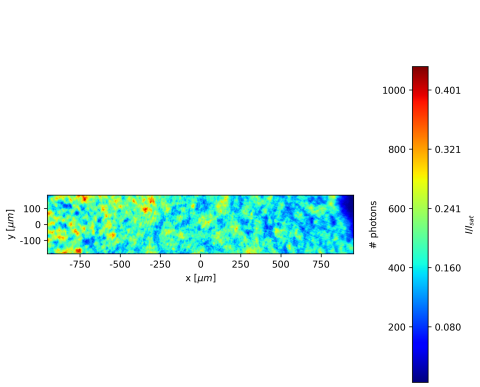

(a) Mean

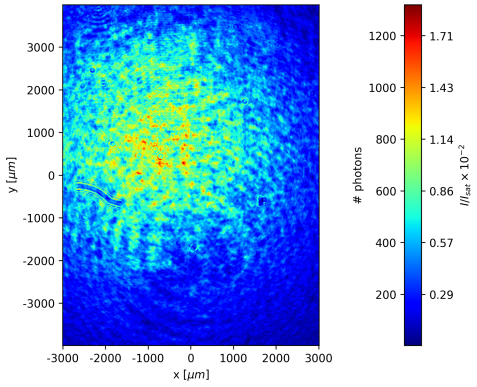

(b) Mean

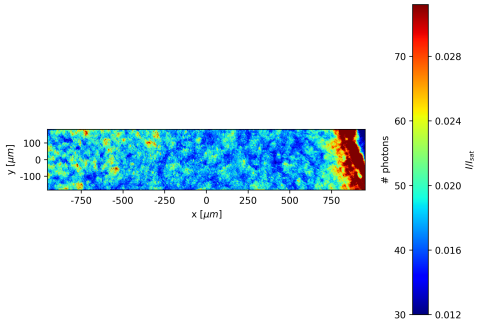

(c) Standard Deviation

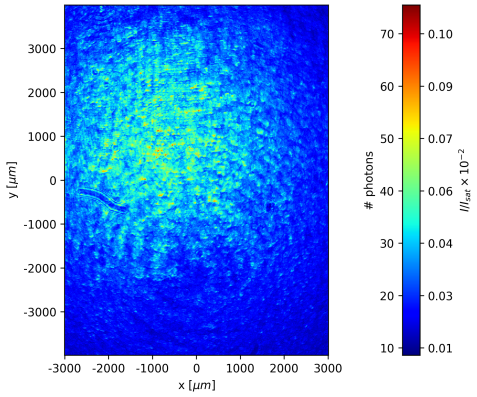

(d) Standard Deviation

Figure 2: Intensity: (a, c) Andor camera at $t_{\text{pulse}} = 8.4\,\mu\text{s}$, $\lambda = 671\,\text{nm}$, $I_{\text{sat}} = 25.4\,\text{W/m}^2$; (b, d) Ximea camera at $t_{\text{pulse}} = 3.0\,\mu\text{s}$, $\lambda = 671\,\text{nm}$, $I_{\text{sat}} = 101.6\,\text{W/m}^2$.

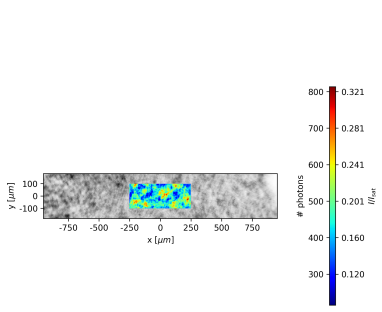

(a) Andor

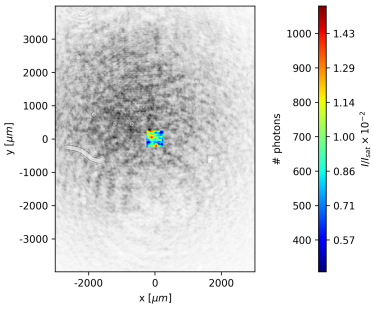

(b) Ximea

Figure 3: Mean intensity and photon number in the region of interest

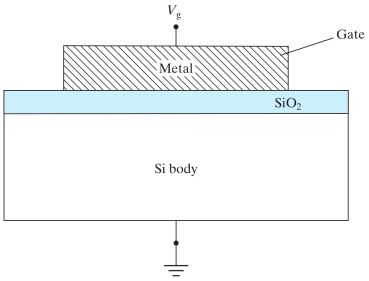

(a) Structure of a MOS capacitor. Figure reproduced from [Hu, 2010].

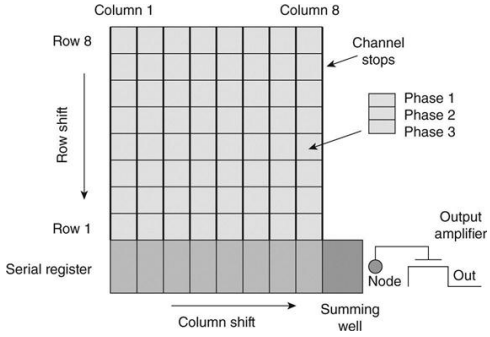

(b) Sketch of a CCD register array. Figure reproduced from [Durini, 2014].

4 CCD Cameras

In this chapter we give a brief overview of the working principles of CCD cameras. Following this we consider different sources of noise during the image creating process and discuss their relevance. Finally, we present the implementation of this discussion in simulations.

4.1 Basic Working Principles

CCD (charge coupled devices) cameras consist of large arrays of individually controlled photodiodes. The photodiodes can register charges created by incident photons due to the photoelectric effect. The read-out electronics produces a voltage pulse proportional to the number of stored charges for each pixel. These voltage pulses are subsequently converted into digital units by an analog-to-digital circuit (ADC). These digital counts then constitute the final image data [Konnik and Welsh, 2014].

The photodiodes used for CCD cameras work similar to metal-oxide-semiconductor (MOS) capacitors (cf. Fig. 4a). In our experiment, as in most applied settings, the cameras are based on a Si substrate. A voltage is applied across two electrodes placed on the metal and the bottom of the semiconductor material. If the voltage is chosen appropriately a potential well forms on the semiconductor side of the oxide-semiconductor interface. The region is depleted of charges. An incident photon can create an electron-hole pair with the electron captured in the potential well. Electron-hole pairs can equally be created due to thermal fluctuations in the depletion area and contribute to the electron count of the pixel. We consider this issue later once we discuss the *dark current noise* [Saleh and Teich, 2013].

After the photoelectrons are captured by the pixels the pixels need to be read-out. The array is made up of a rectangular grid of N columns $\times M$ rows of pixels. For the read-out the single rows are moved sequentially to a serial register situated at one of the edges of the pixel array (s. Figure 4b. The read-out amplifier is located at one end of this serial register and reads-out each pixel one after another. After a row is read all registers shift by a single register along the columns towards the serial register. At the output amplifier the number of electrons produce a potential difference across a capacitance which is measured. This voltage is then first passed through the output amplifier (usually a MOSFET transistor) and then passed to the analog-to-digital circuit.

This process repeats until all pixels are read-out. If the whole pixel array is read-out at once the process is called a frame read-out. Another technique, in use for on of our cameras, is the frame transfer method. In this case a section of the pixel array is covered by an opaque

mask. After capturing an image on the exposed section of the array, instead of a read-out of the pixels, the pixels are just shifted to the registers underneath the mask. As the shifting of registers is considerably faster than the read-out this allows capturing images at higher frame rates [Durini, 2014].

4.2 Noise

Quantum Efficiency The process of photon absorption and electron-hole pair creation and capture is probabilistic. In the case of a photodiode the *quantum efficiency* (QE) is defined as the probability that "a single photon incident on the device generates a photocarrier pair that contributes to the detector current". In the case of a CCD array the probability that a single photon incident generates a photocarrier pair that contributes to the detector count. For a large photon number the QE then corresponds to the ratio of photons incident on a CCD pixel and the electron-hole pairs captured in the pixel.

The deviation of the QE from unity arises due to three processes:

Reflection: At the surface of the device photons may reflect and won't create any electron-hole pairs. This effect is lessened by applying an anti-reflective coating to the surface.

Recombination: Electron-hole pairs may recombine before being read-out by the CCD circuit.

Non-absorption: Photons may pass the pixel without creating any electron-hole pairs at all. The magnitude of this process is governed by the absorption probability and thickness of the material.

Because the above processes depend on the wavelength λ of the incident photon, the quantum efficiency depends on λ as well [Saleh and Teich, 2013].

Photons at short wavelengths, i.e. high energies, might create multiple electron-hole pairs when absorbed by the semiconductor. In our case we, however, only consider light in the infrared region ($\approx 670\,\mathrm{nm}$), with an energy ($\approx 1.85\,\mathrm{eV}$), roughly comparable but above the bandgap energy of Si ($\approx 1.11\,\mathrm{eV}$). Hence, the issue of multiple pair creation doesn't concern us [Durini, 2014]. The quantum efficiency would be modelled by a binomial distribution with the probability p given by the quantum efficiency ≈ 0.9. In our regimes of about $n = 600$ the relative deviation defined by the standard deviation $\sqrt{np(1-p)}$ and mean np is about 0.01. Instead of sampling from the binomial distribution we will therefore just consider the expectation value.

Dark Current Thermal excitations create electron-hole pairs in the pixels. These contribute to the count of the pixel. The mean number of electrons produced per pixel per second is characterized by the dark current I_D. After an exposure time t_{exp} the mean number of electron counts produced is just $N_D = I_D t_{\mathrm{exp}}$. This noise is Poisson distributed with mean N_D. The dark current is temperature dependent and reduces significantly at lower temperatures. Furthermore, due to spatial inhomogeneities in the substrate the dark current has a spatial dependence [Konnik and Welsh, 2014].

In the case of the Andor camera the array is cooled to $T \approx 60\,^{\circ}\mathrm{C}$. At this temperature the dark current is of the order $1\,\mathrm{e}^-/\mathrm{px/s}$. Given an exposure time of the order of $t_{\mathrm{ext}} = 0.3\,\mathrm{ms}$. The order of dark counts is on the order $10^{-2}\mathrm{e}^-$. At this order the dark current is negligible compared to for example the read-out-noise. The Ximea camera on the other hand is not cooled and operates at room temperature. While there is no data on the exact comparison with other data sheets with camera of similar pixel size and substrate yields an estimate of $10^4\mathrm{e}^-/\mathrm{px/s}$ for

the dark current at $T = 30\,^{\circ}\mathrm{C}$. This would imply the dark counts to be on the order $10e^{-}$ for similar exposure times. In this case we expect a contribution of the dark current to the noise. We will discuss the non-uniformity again at the end of this chapter.

Streaking If during the read-out phase the CCD array is still illuminated charges will continue to accumulate on the pixels. Depending on the intensity of the light source as well as the read-out time this can lead to significant distortions of the image. This effect can be circumvented by a shutter [Durini, 2014]. In our experiment the pulse length of the imaging laser is significantly shorter than the exposure time of a single image. Given the experimental set-up stray light is negligible, and we do not expect streaking to affect the image creation process.

Read-Out Noise Before electrons are moved from the serial register to the read-out-node the node is reset to a reference-voltage. The reset voltage has an uncertainty attached due to thermal fluctuations. The uncertainty in the reset voltage leads to an uncertainty of the relative voltage change once the electrons are moved into the node. In modern CCD cameras this issue is ameliorated by correlated double sampling, i.e. measuring the node voltage before and after the electrons are moved to the node [Konnik and Welsh, 2014].

Even though the uncertainty is an uncertainty in the voltage measurement, the uncertainty is commonly quantified in the corresponding uncertainty in the number of electrons. In the case of the Andor and Ximea cameras these values are of the order $10e^{-}$. In the case of the Andor, this implies that besides photon-shot-noise the read-out noise is the most significant source of noise in the set-up. For the Ximea on the other hand the read-out noise is comparable to the dark current noise and needs to be taken into account.

Analog-To-Digital Circuit Noise The output voltage pulse of the sensing node will be amplified and subsequently mapped to a voltage to an integer digital count. For an N bit encoding there can be a maximum of 2^N possible intervals. Usually, before mapping to the voltage bins a bias voltage V_{bias} is added to ensure that all electron count values are mapped onto the bins. This bias count is removed by subtracting from the image a dark image obtained at the same camera settings. Furthermore, the voltage difference of a single electron count V_{e^-} does not necessarily match the voltage interval distance V_i. The ratio

$$K = \frac{V_i - V_{bias}}{V_{e^-}} \tag{37}$$

is referred to as the gain of the camera. If the gain is larger than unity and not an integer one electron count does not correspond to one digital count then [Konnik and Welsh, 2014].

Uniformity and Linearity In an ideal case the digital counts would be exactly proportional to the number of photons incident on the array. The reasons for the non-linear behaviour are mainly twofold. First, a photon-response-non-uniformity (PRNU) is present if the pixels, for example, differ in their quantum efficiencies. Second, a dark-current non-uniformity (DCNU) is present if the dark-current varies between pixels. These two non-linearities are however easily dealt with in post-processing. The DCNU is removed by subtracting a dark image of the same exposure time from the actual image. The PRNU can be eliminated by dividing the image of interest by an image illuminated by the same light source. We need to consider, however, that while these division and subtraction schemes remove the non-uniformity error on average the noise associated with each pixel might still differ. This issue will be further discussed in 4.3, when discussing the implementation of the noise in code.

Last, different voltages and currents might be amplified differently during the analog-to-digital and read-out process. Also the final voltage might not be mapped perfectly linearly onto the digital bins. This behaviour is more difficult to remove from an image as well as to simulate. While approximations are possible (cf. [Konnik and Welsh, 2014]), the precise measurement of the non-linearity is difficult. The corresponding quantity is the integrated linearity error (ILE). This error is calculated as the integral of the deviation of digital counts to photons plot from a straight line up until the full-well-capacity. The upper bound provided by the manufacturers of the cameras in the data sheets is $< 1\%$. In the case of the Ximea, we detect about 600 photons during imaging the relative uncertainty ($\approx 4\%$) due to the photon-shot-noise is significantly larger than the ILE. At lower photon count the ILE becomes even less important. This does not consider other sources of noise adding to the photon-shot-noise. Hence, both PRNU and DCNU are removed by the imaging procedure and the ILE is negligible in our case. Therefore, we will only consider the linear response for the rest of our analysis.

4.3 Code Implementation

While the above discussion is far from complete, we will restrict the simulation of noise to photon-shot-noise (PSN), dark-current-noise (DCN), read-out-noise (RON) and analog-to-digital-conversion-noise (ADCN). We will also consider the quantum efficiency during the process of image creation, but only as a constant and not as a probabilistic process. An overview of the image creation sequence as implemented in the simulation is given in Figure 5. We will consider the different steps separately.

Initially (Step I), a mean intensity per pixel is calculated from a given light source and cloud density profile. In the case of the absorption image this includes the absorption process. For the dark images no light source is present. The only light source considered in the simulation is the imaging laser as we assume stray light to be negligible.

In Step II the mean number of photo-electrons captured in the pixel is calculated for each pixel by

$$\bar{N}_{e^-,\mathrm{ph}} = \frac{I t_{\mathrm{pulse}} A_{\mathrm{px}} QE}{E_\lambda} \tag{38}$$

with I the light intensity, t_{pulse} the pulse length of the imaging laser (the intensity is assumed to be constant), the pixel area A_{px}, QE the quantum efficiency and $E_\lambda = hc/\lambda$ the energy per photon of the imaging laser at wavelength λ. For each pixel the number of photoelectrons is drawn from a Poisson distribution defined by the pixel mean photoelectron number.

$$N_{e^-,\mathrm{ph}} = \mathcal{P}\left(\bar{N}_{e^-,\mathrm{ph}}\right) \tag{39}$$

Even if $\bar{N}_{e^-,\mathrm{ph}}$ is not an integer, $N_{e^-,\mathrm{ph}}$ will be an integer number of photoelectrons.

In Step III the noise sources internal to the camera (excluding adc rounding) are added to the image. For this step two methods are considered. First, an explicit implementation of the DCN and RON. Second, a more heuristic method discussed later.

The number of electrons captured in a pixel due to dark currents is determined by drawing from a Poisson distribution

$$N_{e^-,\mathrm{dc}} = \mathcal{P}(\bar{N}_{e^-,\mathrm{dc}}), \quad \bar{N}_{e^-,\mathrm{dc}} = i_{\mathrm{dc}} t_{\mathrm{exp}} \tag{40}$$

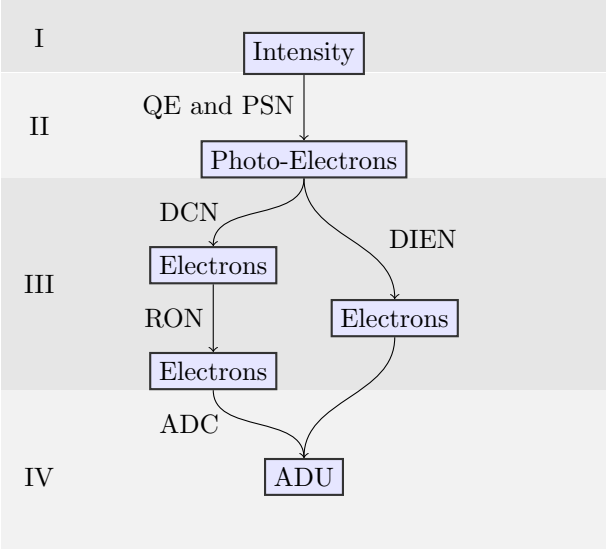

Figure 5: Sketch of the simulation noise sequence: (QE) quantum efficiency, (PSN) photon-shot noise, (DCN) dark-current noise, (RON) read-out noise, (ADC) analog-to-digital conversion, (DIEN) dark-image extracted noise.

where i_{dc} is the dark current in $\mathrm{e}^-/\mathrm{px/s}$ as determined, for example, from the manufacturers data-sheet for a given working temperature. t_{exp} is the exposure time of the camera. The read-out time is considered short with respect to the exposure time, such that streaking due to dark noise can be neglected.

After the DCN the read-out noise is applied to the image. The read-out noise is modelled as a normal distribution. The mean corresponds to the bias voltage and the variance describes the uncertainty in the voltage measurement by the serial node.

$$N_{e^-,\mathrm{ro}} = \mathcal{N}(N_{e^-,\mathrm{bias}},\ \sigma_{e^-,\mathrm{ro}}) \tag{41}$$

In the simulation both are input in units of e^-, as provided by the manufacturer. For both, the DCN and RON, a spatially fixed pattern could be introduced.

This then yields the electron count as measured by the read-out node.

$$N_{e^-} = N_{e^-,\mathrm{ph}} + N_{e^-,\mathrm{dc}} + N_{e^-,\mathrm{ro}} \tag{42}$$

Before considering the analog-to-digital step we discuss another heuristic method of introducing noise.

As described in 4.4, we can approximate the overall noise associated with the camera from a set of dark images taken at a set camera setting and exposure time. We call this the dark-image extracted noise (DIEN). This provides a second methods to model the camera noise. In the simulation the noise profile is input at the read-out stage with the dark current set to zero.

Last, the electron count is converted to digital units (ADU). For a given camera setting this value is provided by the manufacturer. The value is usually referred to as the sensitivity or (e^-/ADU)

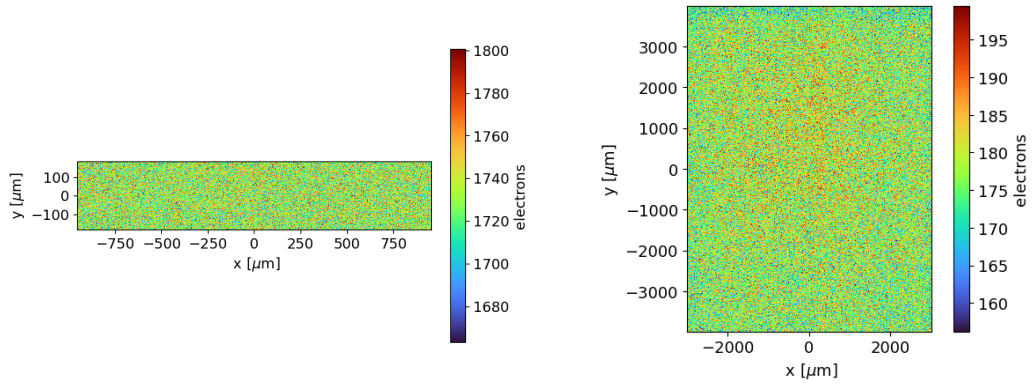

(a) (b)

Figure 6: Example dark images in units of electrons. (a) Andor: $N_{\text{images}} = 11023$, $t_{\text{exp}} = 300\,\mu\text{s}$, $T_{\text{CCD}} \approx -80\,^{\circ}\text{C}$. (b) Ximea: $N_{\text{images}} = 2038$, $t_{\text{exp}} = 250\,\mu\text{s}$, $T_{\text{CCD}} \approx 30\,^{\circ}\text{C}$.

or acquisition gain (ADU/e^-). As the final data is given in integer counts the result will be rounded as well.

$$N_{\text{ADU}} = \text{round}\left(\frac{N_{e^-}}{\text{sensitivity}}\right) \tag{43}$$

This value then constitutes the final image data.

4.4 Modelling Noise From Dark Images

From the experiment we have a set of dark images given for both the Andor ($N = 11023$) and the Ximea camera ($N = 2308$). Example dark images are depicted in Figure 6b and 6a and for both cameras.

The conversion of ADU to electrons is given by the sensitivity:

$$N_{\text{ADU}} \cdot \text{sensitivity} = N_{e^-} \tag{44}$$

where we neglect any rounding.

When analysing the noise we are interested in the variation of pixel counts across multiple images instead of the variation across a single image, because each pixel has a potentially different noise profile. The mean and standard deviation of each pixel are shown in Figure 7. The colour scale represents the 3σ interval centred at the mean. For both cameras different spatial patterns are visible in the mean images. In case of the Andor the spatial structure is aligned along the rows and columns of the CCD array and varies by about $2\,\text{e}^-$ across the image, a small variation considering the standard deviation between images is on the order of $22\,\text{e}^-$. In the case of the Ximea the pattern appears more fringe-like. The variation of the mean across the image is about $60\,\text{e}^-$, compared to a standard deviation between the images of about $13\,\text{e}^-$ Furthermore, on the Ximea, defects are visible in some areas. The mean value is mainly determined by the bias voltage of the CCD camera, as it does not fluctuate it can be removed from the final image by subtraction of the dark image. The observed noise is contained in the image-to-image variation in the dark count, which we characterize by the variance, as shown in Figure 7c and 7d.

For the Andor some "hot-pixels" can be distinguished as dark dots. The 10 pixels with the highest variance have an average standard deviation of $57.8\,\mathrm{e}^-$, with the largest variance with a standard deviation of $197\,\mathrm{e}^-$. The variance of dark counts for the Andor matches well with the read-out-noise as provided by the data sheet ($\sigma_{e^-,\mathrm{ro}} = 22.6\,\mathrm{e}^-$). Due to the low cooling temperature of the Andor ($T_{\mathrm{CCD}} \approx -80\,^\circ\mathrm{C}$), the dark current count should be on the order of $i_{\mathrm{dc}} = 0.01\,\mathrm{e}^-/\mathrm{px/s}$. For exposure times of about $t_{\mathrm{exp}} = 300\,\mu\mathrm{s}$ the dark current is therefore negligible.

For the Ximea, the variance in dark count is an order of magnitude lower than the Andor. The noise, as estimated from the variance, turns out to be lower than the data-sheet value for the read-out noise ($\sigma_{e^-,\mathrm{ro}} = 68\,\mathrm{e}^-$). While there is no manufacturer value provided we expect a contribution due to dark-current noise, as the camera operates above room temperature ($T_{\mathrm{CCD}} \approx 30\,^\circ\mathrm{C}$). After correcting for the pixel size we can obtain a rough estimate for the dark noise from the Andor dark current at the same temperature ($i_{\mathrm{dc}} = 1200\,\mathrm{e}^-/\mathrm{px/s}$). For the exposure time of the Ximea this suggests a dark current noise on the order of $0.5\,\mathrm{e}^-/\mathrm{px}$. For the Ximea we observe a correlation between the mean and variance of the dark images. Considering, the dark noise variation is of the same order as the data-sheet value, it is unlikely that this is due to stray light. The variance differs across the image by about $2\,\mathrm{e}^-/\mathrm{px}$, which could be accounted for by a variation in the dark current.

4.4.1 Maximum-Likelihood-Estimate

We next want to model our noise by considering the dark images. We consider the normal distribution, as expected from the read-out noise. The parameters for the distributions are estimated by means of the Maximum-Likelihood-Estimate. The following introduction to the Maximum-Likelihood-Estimate is summarized from [Almudevar, 2021].

Given a parametric family of probability densities $\mathcal{P} = \{p_\theta : \theta \in \Theta\}$, with p_θ a probability distribution parametrized by θ from the parameter space Θ. For example in the case of a normal distribution, $\theta = (\mu, \sigma^2)$ and $p_\theta(x) = \frac{1}{\sqrt{2\pi\sigma^2}} \exp\left(\frac{(x-\mu)^2}{2\sigma^2}\right)$. Then given a set of independent observations $X = \{X_1, X_2, ..., X_n\}$ the likelihood of the observation for a given distribution of the parameter family is

$$\mathcal{L}(\theta; X) = \prod_{i=1}^{N} p_\theta(X_i) \tag{45}$$

where we now consider $\mathcal{L}$ to be a function of θ for a fixed observation X. In practice the log-likelihood is computationally more amenable

$$\ell(\theta; X) = \log \mathcal{L}(\theta; X) = \sum_{i=1}^{N} \log p_\theta(X_i) \tag{46}$$

The *Maximum-Likelihood-Estimate* (MLE) is in turn defined by maximising the likelihood for a given set of observations

$$\hat{\theta} = \mathrm{argmax}_{\theta\in\Theta}\ \mathcal{L}(\theta; X). \tag{47}$$

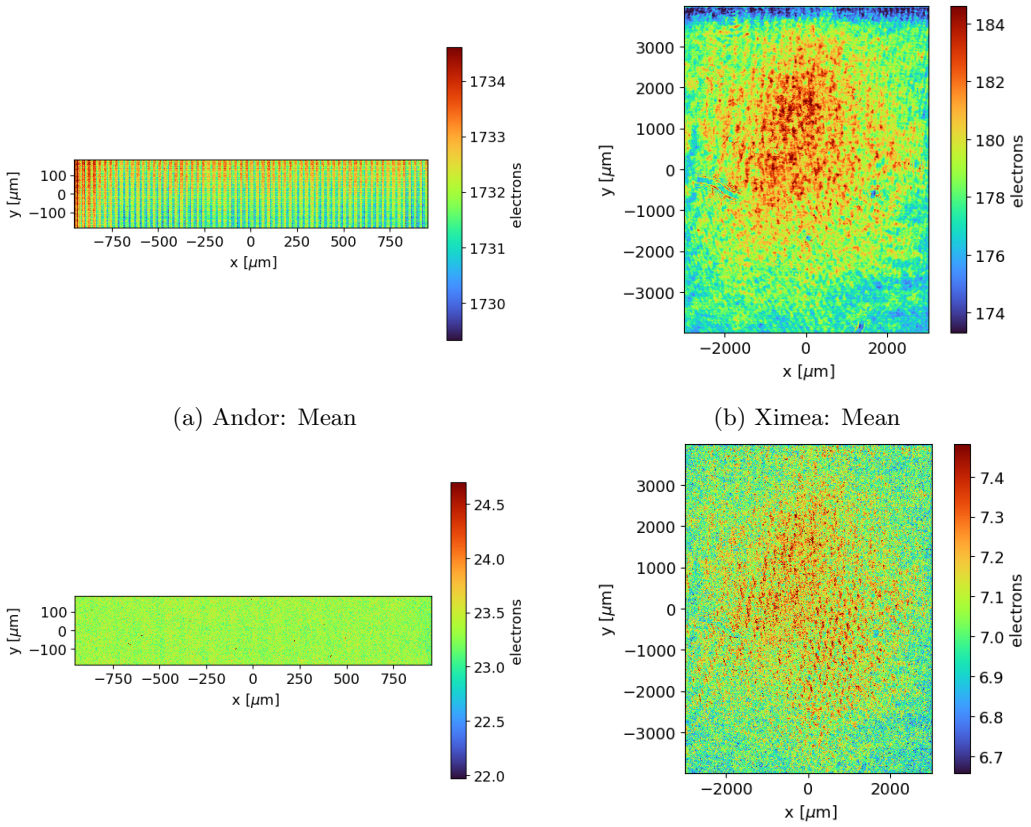

(a) Andor: Mean

(b) Ximea: Mean

(c) Andor: Standard Deviation

(d) Andor: Standard Deviation

Figure 7: Mean and standard deviation of dark image counts in units of electrons. Andor (left): $N_{\text{images}} = 11023$, $t_{\text{exp}} = 300\,\mu\text{s}$, $T_{\text{CCD}} \approx -80\,^{\circ}\text{C}$. Ximea (right): $N_{\text{images}} = 2038$, $t_{\text{exp}} = 250\,\mu\text{s}$, $T_{\text{CCD}} \approx 30\,^{\circ}\text{C}$.

In the case of the normal distribution the log-likelihood is given by

$$\ell(\mu, \sigma; X) = -N \log\left(\sqrt{2\pi}\sigma\right) - \frac{1}{2\sigma^2} \sum_{i=1}^{N} (X_i - \mu)^2 . \tag{48}$$

The MLE parameter can then be found explicitly as

$$\mu = \bar{X} \tag{49}$$

$$\sigma^2 = \frac{1}{N} \sum_{i=1}^{N} (X_i - \bar{X})^2. \tag{50}$$

4.4.2 Maximum-Likelihood-Estimate Analysis of the Dark Images

Due to the dominance of read-out noise, as discussed for the dark images, we expect the noise to be modelled by a normal distribution. While the optimal parameters for the MLE of the normal distribution can be computed directly as the sample mean and variance we want to convince ourselves that the noise is indeed modelled by a normal distribution. In Figure 8 we show a histogram for three different pixels as well as the corresponding normal noise model sampled the same number of times as the number of dark images available.

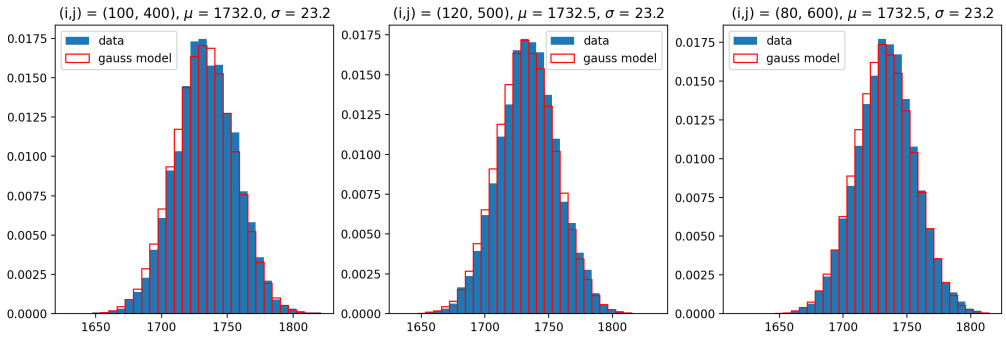

(a) Andor

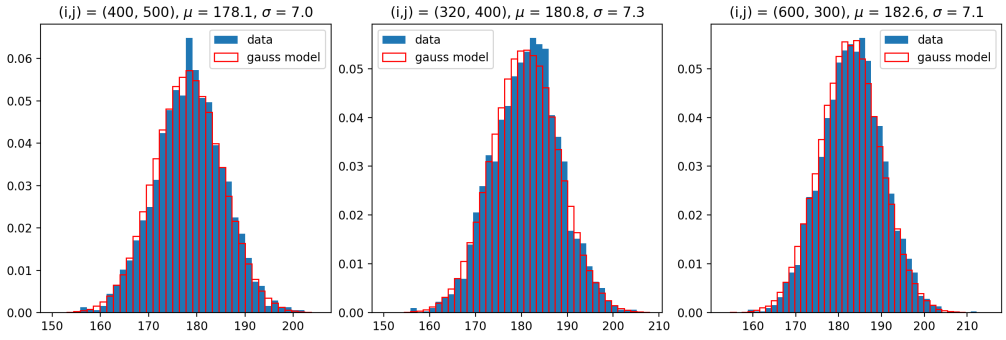

(b) Ximea

Figure 8: Maximum-Likelihood-Estimate: Results for three different pixels.

In both cases the normal distribution appears to approximate the noise distribution well. To obtain a rough estimate about the validity of the normal model we additionally check for numerical convergence of the MLE. Convergence is defined by convergence of the `scipy.maximise` function after 1000 iterations with initial parameters given by the optimal MLE parameters. The convergence test was performed for 100 randomly selected pixels in the region of interest. In the case of the Andor the MLE converged numerically in 78/100 cases and in case of the Ximea in 75/100 cases.

Due to these results we decided to model the dark-current and read-out noise in the simulation by a normal distribution with mean and variance provided by the dark images. While this removes a small contribution due to the counting statistics of the dark current, it allows to capture some of the spatial variation in the noise profile. We decided this to be a more accurate model of the camera noise. When in the following we present simulated images with noise applied, unless explicitly mentioned otherwise, the normal noise profile with local mean and variance is used.

5 Simulation and Data Analysis

During a run of the experiment we usually collect a set of images of our atomic clouds for given experimental settings. These settings consist of a choice of camera and noise profile (Chapter 4), a light source (Chapter 3) and a cloud model (Chapter 2). Afterwards, we fit a theoretical model to the density profile to obtain fit-parameters which constitute our knowledge about the cloud. It is this process which we try to model. In this section we will therefore discuss different parts of the experimental set-up and the chosen model for our simulation. Once we set up our model we can create images of the atomic clouds and subsequently perform a fitting routine and post-processing to arrive at our final set of data. This data is then in turn compared to the input parameter of the simulated clouds to deduce the effect of different experimental settings and sequences on the fit accuracy. By creating large sets of input images we can obtain statistics about these effects.

In this chapter we consider the set of cloud parameters for which we run the simulations. In the following we call a series of simulations run for a subset of the parameter space, e.g. the T/T_{F} parameter, a sweep.

5.1 Image Creation

To create a density image according to Equation 34 we need to simulate at least three different images. For each we first calculate the mean intensity incident on each pixel, before calculating the corresponding image in digital units output by the camera. For the purposes of our simulation we consider the intensity constant across the area of a single pixel. This is, however not exactly true for the atomic cloud densities. In the case of the absorption image the intensity is therefore not determined by the density at the pixel centre alone. A better approximation is given by the pixel average density (cf. Appendix C).

For the dark images zero intensity is incident on the camera. Similar to the experiment, in the case of the Andor, we create 6 dark images, which we average to obtain a single dark image. In the case of the Ximea a single dark image is used.

In Figure 9 an example density image from the experiment and the corresponding simulated image is shown. They are normalized by subtracting the mean density in the far regions.

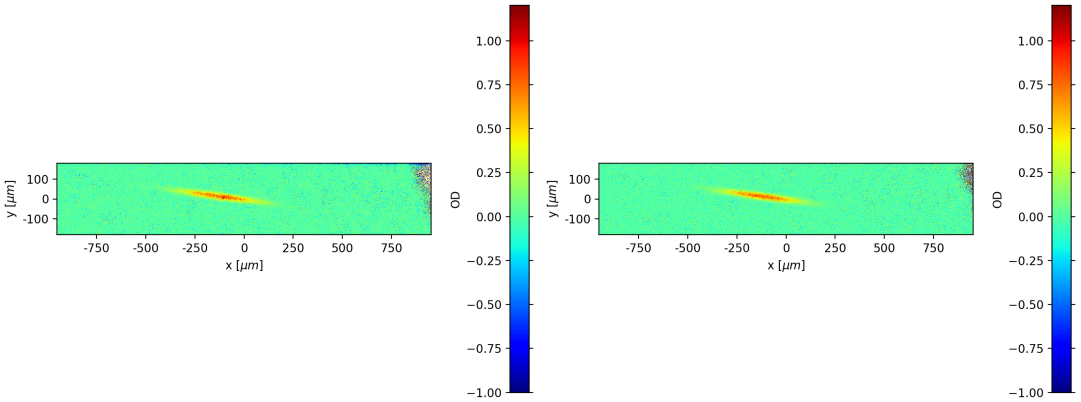

(a) Experiment (b) Simulation

Figure 9: A density image obtained from (a) the experiment and (b) the simulation. The input parameter for the simulation are the fit results of the experimental image: $n_{2D0} = 3.6e12m^{-2}$, $T/T_F = 0.32$, $R_x = 12\,\mu$m, $R_y = 149\,\mu$m.

5.2 Sweep Parameter Choice

The cloud column density profiles we consider are either the thermalised Boltzmann (8) or Fermi gas (4). We describe these gases either in-situ (Chapter 2.1) or during expansion (Chapter 2.3). We will assume to be able to image the clouds instantaneously, i.e. no blurring due to movement within the cloud or due to expansion of the cloud. This is justified for the given pulse lengths of our imaging lasers as discussed in [Filzinger, 2018].

The 3D density of the Fermi gas in-situ is fully determined by specifying the atom number N, the temperature T and the trap frequencies ω_x, ω_y and ω_z (Equation (4) and 6). For the time-of-flight experiment the expansion time t_{TOF} is added as an independent parameter.

We were provided an already analysed set of data by the lab group, from which we deduced an average atom number $N = 35000$ and temperature $T = 250\,$nK. The trapping frequencies of the optical trap were measured by an independent measurement [Freund, 2022] as

$$\omega_{rad} = 2\pi\,1878\,\text{Hz}, \quad \omega_{ax} = 2\pi\,32\,\text{Hz} \tag{51}$$

where ω_{rad} is the radial component of the trap and ω_{ax} the axial component. They are related to the camera $x - y$ axes as

$$\omega_x = \omega_{ax}$$
$$\omega_y = \omega_{rad}$$

for the Andor set-up and

$$\omega_x = \frac{\omega_{\mathrm{rad}}\omega_{\mathrm{ax}}}{\sqrt{\omega_{\mathrm{rad}}^2 \sin^2(40°) + \omega_{\mathrm{ax}}^2 \cos^2(40°)}}$$
$$\omega_y = \omega_{\mathrm{rad}}$$

for the Ximea set-up, as described by Equation (21).

If we consider the column density of the Fermi gas in-situ, the cloud (18) is parametrized by $n_{2\mathrm{D}0}$, R_x, R_y and q. This set of parameters can be completed by adding the parameter ω_z. The various relation between this set of quantities and the set of quantities above are detailed in chapter 2. We are therefore free to either specify N, T and ω_x, ω_y, ω_z or the column density quantities.

One experimental parameter of great interest is the T/T_{F} parameter. We want to perform a sweep for the range $T/T_{\mathrm{F}} \in [0, 1]$. As discussed before our density profile isn't fully specified by only determining T/T_{F}. To choose the other parameters we realize, that the density features prominently in the Beer-Lambert law. We therefore want to ensure, that the result in the fit accuracy isn't mostly due to the density, rather than the T/T_{F} parameter we are interested in. Furthermore, we consider the trap frequency fixed, which provides a further constraint. For this reason, we calculate the peak density (17) as given by the experimental input parameters as $n_{2\mathrm{D}0}(t=0) = 18.8 \times 10^{12}\,\mathrm{m}^{-2}$ for the Andor and $n_{2\mathrm{D}0}(t=0) = 29.9 \times 10^{12}\,\mathrm{m}^{-2}$ for the Ximea camera. For a specific T/T_{F} this provides us with a total of 5 parameters which fully specifies our cloud in-situ. Due to the scaling behaviour of $R_i^2(t) = R_i^2(0)(1+\omega_i^2 t^2)$, and N and T/T_{F} being constant during the TOF, the peak density (17) stays the same for all T/T_{F} for all times t.

In Figure 10, we provide a overview of the relation of the various cloud parameters for this choice of parameters. Additionally, one choice of a higher and lower density is shown. Later, we will perform the sweep for a set of different densities, to see the resolution limit for the different cameras. The scaling relation holds for all choices of peak density.

5.3 Fitting Routine

To obtain physical quantities from the absorption images we need to fit a model to the data. Due to the scaling of the cloud in the TOF expansion we can fit both, in-situ and expanded clouds, with the same fit functions. As in the limit of large T/T_{F} the Fermi density distribution becomes Gaussian the fit of the Gaussian provides some characterization of the cloud as a Boltzmann gas. In our fit we make use of two different fitting functions:

$$n_{2\mathrm{D,fit}}(x,y; n_{2\mathrm{D}0}, q, R_x, R_y, \mu_x, \mu_y, \theta, n_{\mathrm{offset}}) = n_{2\mathrm{D}0}\frac{\mathrm{Li}_2\left(-\exp\left[q - \left(\frac{x'^2}{2R_x^2} + \frac{y'^2}{2R_y^2}\right) f(\mathrm{e}^q)\right]\right)}{\mathrm{Li}_2\left(-\mathrm{e}^q\right)} + n_{\mathrm{offset}} \tag{52}$$

$$n_{G,2\mathrm{D,fit}}(x,y; n_{2\mathrm{D}0,G}, \sigma_x, \sigma_y, \mu_x, \mu_y, \theta, n_{\mathrm{offset}}) = n_{2\mathrm{D}0,G}\exp\left(-\frac{x'^2}{2\sigma_x^2} - \frac{y'^2}{2\sigma_y^2}\right) + n_{\mathrm{offset}} \tag{53}$$

Where (x', y') describe the coordinate system of the cloud and (x, y) the coordinate system of

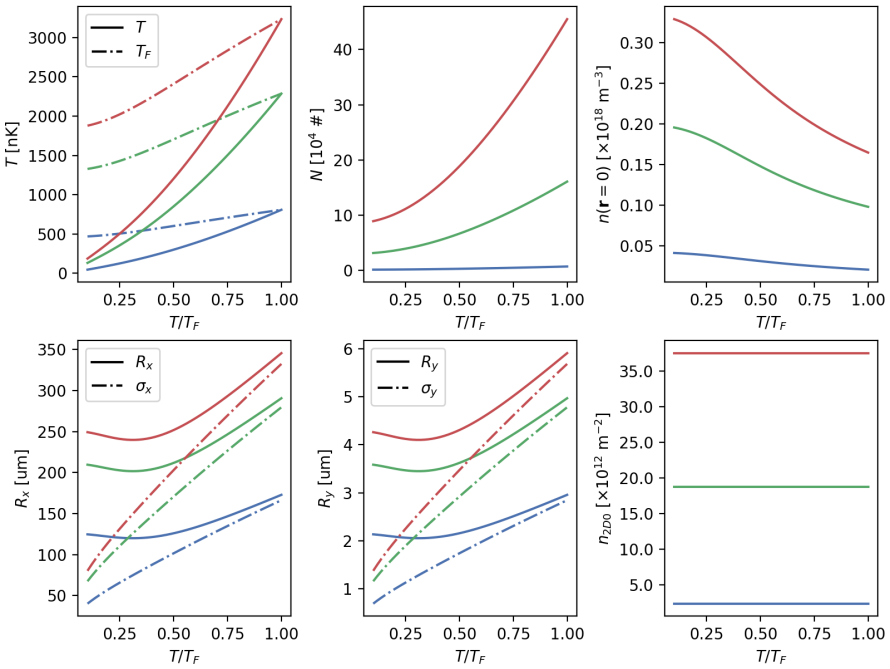

Figure 10: In-situ cloud parameter for T/T_F sweep for different peak densities and constant trap frequencies $\omega_x = 2\pi\,32\,\mathrm{Hz}$, $\omega_y = 2\pi\,1878\,\mathrm{Hz}$, $\omega_z = 2\pi\,1878\,\mathrm{Hz}$ for the Andor camera. — $n_{2\mathrm{D}0} = 2.35 \times 10^{12}\,\mathrm{m}^{-2}$, — $n_{2\mathrm{D}0} = 18.77 \times 10^{12}\,\mathrm{m}^{-2}$, — $n_{2\mathrm{D}0} = 37.54 \times 10^{12}\,\mathrm{m}^{-2}$.

the CCD array. They are related by:

$$\begin{pmatrix} x' \\ y' \end{pmatrix} = \begin{pmatrix} \cos\theta & \sin\theta \\ -\sin\theta & \cos\theta \end{pmatrix} \begin{pmatrix} x \\ y \end{pmatrix} - \begin{pmatrix} \mu_x \\ \mu_y \end{pmatrix} \tag{54}$$

In the experiment, the cloud isn't perfectly centred and the angular and spatial are required for a proper fit. In our simulation we choose a slight spatial offset ($\pm 2\,\mu$m), to avoid that the cloud is perfectly centred on a single pixel. The fit routine we use for cloud images is composed of two steps. First, we fit a Gaussian to the image. The Gaussian fit provides an initial estimate for the cloud size, position, angle, peak density and offset. Second, we fit the Fermi column density with initial parameters provided by the Gaussian.

The Gaussian fit is initialized by the parameters

$$\begin{aligned} n_{\mathrm{2D0}} &= \max(I_{n_{\mathrm{2D}}}) - \mathrm{mean}(I_{n_{\mathrm{2D0}}}) \\ \sigma_x &= 50\,\mu\mathrm{m} \\ \sigma_y &= 50\,\mu \\ \mu_x &= 0.0\,\mu\mathrm{m} \\ \mu_y &= 0.0\,\mu\mathrm{m} \\ \mathrm{offset} &= \mathrm{mean}(I_{n_{\mathrm{2D0}}}). \end{aligned}$$

The Fermi fit is additionally provided with an initial guess for q corresponding to $T/T_{\mathrm{F}} = 0.5$. As discussed in the appendix Appendix B we use a sufficiently accurate spline approximation for the polylogarithm function. The spline implementation is about three orders of magnitude faster than exact implementations (e.g. the `mpmath` Python library). If the fit routine does not converge a NaN result is returned, which is taken care of during the post-processing.

In the case of the TOF expansion, after we obtain the cloud size fit parameter, they are fitted by the expansion formula:

$$f_{\mathrm{TOF}}(t; a, b) = \sqrt{a + bt^2} \tag{55}$$

The parameter a corresponds to $\sigma_i^2(t = 0)$ or $R_i^2(t = 0)$ depending on whether we use the Gaussian or Fermi sizes. The second parameter b is proportional to the temperature. In the case of the Gaussian size $b = k_{\mathrm{B}}T/m$ and in the Fermi case $b = k_{\mathrm{B}}Tf(\mathrm{e}^q)/m$. The Fermi case, therefore, requires an estimate of q to obtain T. The error is propagated from b and q to T, via Gaussian error propagation. We can then use the temperature estimate to calculate T/T_{F} by calculating T_{F} from the atom number and mean trapping frequency as described by (12). Another method, which we will call the 'direct method' is to calculate T/T_{F} from the obtained q fit parameters for all TOF images and determine T/T_{F} from the mean with the uncertainty given by the standard deviation.

5.4 Post Processing

Depending on the noise and density regime the fits of the Fermi and Gauss column densities, might not converge or converge with large uncertainties in their fit parameters. We decided to remove fit parameters with large uncertainties attached to them or outliers with fit parameters orders of magnitude removed from the actual parameters. To not bias the analysis the selection procedure is defined the same for all simulation runs discussed in the following chapters. For

single time instance simulations, all fit parameters with a relative fit error larger than 0.2 in the n_{2D0}, R_x and R_y were discarded. The relative error in q is not considered, due to the exponential relationship with T/T_F. This error was determined by calibrating the T/T_F sweep for $t_{TOF} = 0.6$ and $n_{2D0}(t = 0) = 37.6 \times 10^{12}\,\mathrm{m}^{-2}$ with the Andor camera to provide a good accuracy in the T/T_F parameter. For time-of-flight series the procedure is slightly more complicated to avoid discarding all data points.

1. If more than 60% of all data points fulfil the 0.2 relative error threshold, remove all values with higher relative error.
2. If less than 60% of all data points fulfil the relative error threshold, increase the threshold by 0.1, repeat.
3. Remove all time steps with a relative deviation in the cloud size parameter R_i greater than 0.7.

This procedure allows keeping enough data points to fit a time-of-flight fit function. No data points were removed individually.

5.5 Principal Component Analysis

Instead of removing data points with high fit uncertainties, one can try to reduce the overall noise in the images before performing the fit. We present one such method, the principal component analysis, in this section. We consider our final density images to represent a p-dimensional image, with p the number of pixels, with the basis vectors represented by single pixel. For our atomic clouds, the density values in one pixel will be correlated with the density values in the neighbouring pixels, whereas they won't be correlated with density values of pixels far removed. Hence, the basis vectors in the "pixel basis" are not statistically independent. The principal component analysis provides a procedure to find a different set of basis vectors, which are statistically independent [Segal et al., 2010]. In the ideal case each variation of an independent experimental parameter, e.g. N, or T, will have a single associated basis vector. All basis vectors not related to an experimental parameter will then represent noise and can be discarded. The resulting basis vectors (a superposition of pixel basis vectors) can be visualized as images. In practice, due to insufficient statistics and correlation of experimental parameters, the new basis vectors don't correspond to only one feature and still contain some noise. This will be discussed in the results chapter. The new basis is determined by the following algorithm:

Consider a set of n images $X = \{X_1, \ldots, X_n\}$, each consisting of p pixels. The mean image is denoted by

$$\bar{X} = \frac{1}{n}\sum_{i=1}^{n} X_i \tag{56}$$

such that each image is decomposed as

$$X_i - \bar{X} = Y_i = Y_{i,1}e_1 + \ldots Y_{i,p}e_p \tag{57}$$

with e_k the kth pixel basis vector and $Y_{i,k}$ the coefficient of the kth pixel basis vector for the ith image. The covariance matrix S is of dimension $p \times p$ and constructed as

$$S_{jk} = \frac{1}{n-1}\sum_{i=1}^{n} Y_{i,j}Y_{i,k}. \tag{58}$$

The diagonal elements of the matrix represent the variance of the pixels and the off-diagonal elements the covariance of different pixels. By diagonalizing the covariance matrix we obtain a new set of basis vectors u_k for which only the diagonal elements remain. The new basis vectors are hence statistically independent and are referred to as the principal components. The diagonal element of S associated with each basis vector (their eigenvalue) determines their explanatory strength for the observed variation between images, as most of the variation between images is assumed to result from the variation of experimental parameters. Because before the basis vectors weren't statistically independent the variance will vanish for all but m of the new basis vectors. The images can then be expressed in the basis as

$$Y_i = Y_{i,1}^P u_1 + \dots Y_{i,m}^P u_m. \tag{59}$$

The components $Y_{i,k}^P$ are calculated by projection on the respective basis vector as

$$Y_{i,k}^P = Y \cdot u_k. \tag{60}$$

In practice, due to noise and insufficient statistics some of the variances will be small even if not zero. In this case it is practical to only choose the basis vectors associated with the l largest variances. The image is then approximated by

$$Y_i \approx Y_{i,1}^P u_1 + \dots Y_{i,l}^P u_l. \tag{61}$$

Most of the information is then contained in l instead of p components, where l is typically significantly smaller (~ 10) than the number of pixels.

In our analysis we used of the `scikit-learn` [Pedregosa et al., 2011] package, which provides a convenient and tested implementation of the PCA algorithm.

6 Results

In this chapter we present the results of the simulation and fitting procedure for different experimental realizations. We first consider the viability of the PCA method to improve the fit accuracy. Subsequently, we discuss the resolution limit due to noise involved in the absorption-imaging process. For this we consider different T/T_{F}, density and cloud size regimes, as well as different simulated imaging-laser sources. Last, we analyse an actual experimental run of a ramp and provide a lower uncertainty bound on the accuracy of the actual fit parameter.

6.1 Principal Component Analysis and Improvement of the Fit Accuracy

By means of the PCA we hope to distinguish correlated from uncorrelated noise. Therefore, we hope to distinguish changes in our cloud shape due to fluctuations in the experimental parameters from the uncorrelated noise involved in the imaging process. For this analysis we choose the atom number N and the cloud temperature T as fluctuating cloud parameters. The atom number mainly influences the overall density (Equation (17)), while the temperature affects the size (Equation (13)). Both change the cloud shape also via T/T_{F}. The fluctuation is modelled by a normal distribution with $\mu_N = 36000$ and $\sigma_N = 3600$ for the atom number and $\mu_T = 278\,\mathrm{nK}$ and $\sigma_T = 14\,\mathrm{nK}$ for the temperature. The two parameters are modelled to fluctuate independently. The cloud is then imaged at early time $t_{\mathrm{TOF}} = 0.6\,\mathrm{ms}$ and late time $t_{\mathrm{TOF}} = 2.1\,\mathrm{ms}$ for the atom number case and only imaged at early time in case of the temperature variation. After the expansion the cloud size is about $R_x = (207 \pm 4)\,\mu\mathrm{m}$, $R_y = (25 \pm 1)\,\mu\mathrm{m}$ at early times and $R_x = (224 \pm 4)\,\mu\mathrm{m}$, $R_y = (87 \pm 2)\,\mu\mathrm{m}$ at late times. Following this we consider simultaneous fluctuations in T and N, as specified before, with an additional fluctuation in the centre position of the cloud of $\sigma_{\mu_x} = 2\,\mu\mathrm{m}$ and $\sigma_{\mu_y} = 2\,\mu\mathrm{m}$. To complement this analysis we present the results of a PCA on a complete TOF series at 12 linearly spaced time steps with fixed N, T and spatial position from $0.2\,\mathrm{ms} - 2.9\,\mathrm{ms}$. In all cases we only consider images simulated with the Andor camera profile. We input noise and light as discussed in 4.2 and 3.3. For the temperature and number variation we consider sets of 40 images each. For the TOF we create 5 images at each time step.

6.1.1 Atom Number Fluctuation

From the PCA we obtain the principal components as explained in 5.5. We want to quantify how the fit accuracy changes after taking into consideration different numbers of the components. For the case of the fluctuation in the atom number the components are displayed as images in Figure 14a. Each image explains a share of the complete variance between the images. The first image explains the greatest share of the variance with 0.032. For all higher order principal components the relative share of the explained variance decreases. In Figure 12 the variance explained by each component is shown. It turns out that in the case of atom number fluctuations the relative explained variance is approximately constant for all component except the first. All components of order higher than 40 vanish, because for 40 images all the variance can be captured by an equal or lower number of principal components.

We know want to quantify the effect of reconstructing the image by taking into account the highest n principal components. One such reconstruction is shown in Figure 11. Going from the first (mean) image to the second the variation associated with the first principal component is added back onto the image. The change is difficult to distinguish from the image alone. For adding back higher order components it becomes clear, that an increasing amount of noise gets

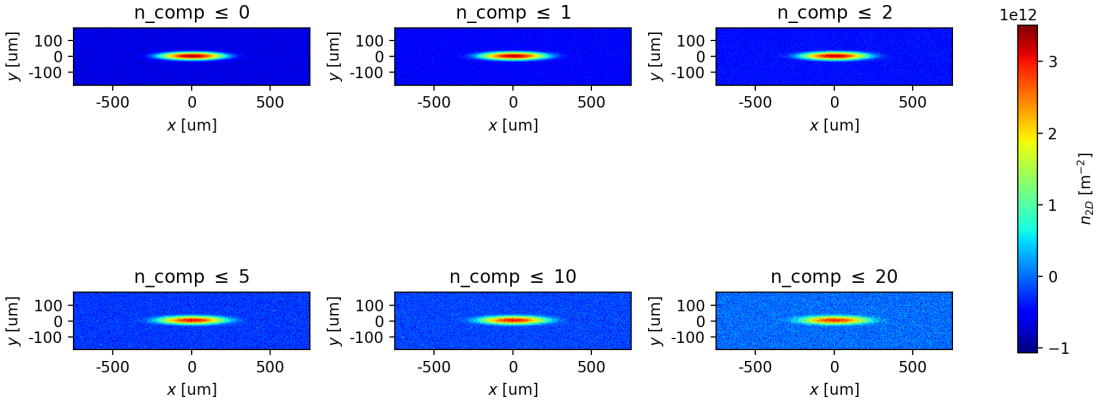

Figure 11: PCA image reconstruction for n principal components. Parameter fluctuation in the atom number $N = (36\,000 \pm 3600)$ at constant temperature $T = 278\,\mathrm{nK}$. Cloud expansion for early times $t_{\mathrm{TOF}} = 0.6\,\mathrm{ms}$.

introduced back into the image.

The cloud parameters for the original and PCA reconstructed images are estimated by the image fitting routine as described in 5.3. The results for the fluctuation in the atom number at early and late expansion time are shown in Figure 13a and 13b. The cloud parameters fluctuate for each of the 40 images. Therefore, we calculate the relative error with respect to the input parameters for each image. The standard deviation and mean of the relative errors then describe the fit accuracy. We additionally consider the fit accuracy of the mean image. In this case we fit the mean image once and then compare these fit parameters with the input parameters.

Overall, the error in the fit parameters relative to the mean input parameter is $\lesssim 10\%$ and the fit accuracy improves compared to the fit without the PCA applied. The fit results are the most accurate when we consider only the first PCA component. Once more components are added, the fit accuracy decreases until it attains the same accuracy as the fit without the PCA applied. This is not surprising as for 40 components all the variation (and thereby all the noise) is added back to the images. The fact that the fit is most accurate after adding only the first component is explained by the principal components in Figure 14. For both early and late times only the first component displays structure, albeit less pronounced for the late time images. In both cases the first component explains a greater share of the total variance compared to components of higher order.

We can equally consider only the mean image ($n = 0$ in Figure 13), without any principal components taken into account. For the N fit parameter the variation in N matches the input variation $\sigma_N = 3600$, which is expected. The accuracy for N is worse than the fit with and without the PCA applied. On the other hand the fit accuracy for T/T_{F} improves with respect to the fit without the PCA applied. Due to the relationship $T/T_{\mathrm{F}} \propto N^{-1/3}$ the 10% variation in N changes the parameter by about 3%. As discussed in Chapter 2 the information about the parameter is mostly contained in the wing shape. As the variation in the parameter is less than the relative error in the plain fit, fitting the mean image improves this result. In the case of the clouds size parameters R_x and R_y, fitting the mean image degrades the fit accuracy for early times, but improves accuracy for late times. The atom number does not change R_i, the different effect on accuracy is therefore due to the relative relevance of noise at lower density compared

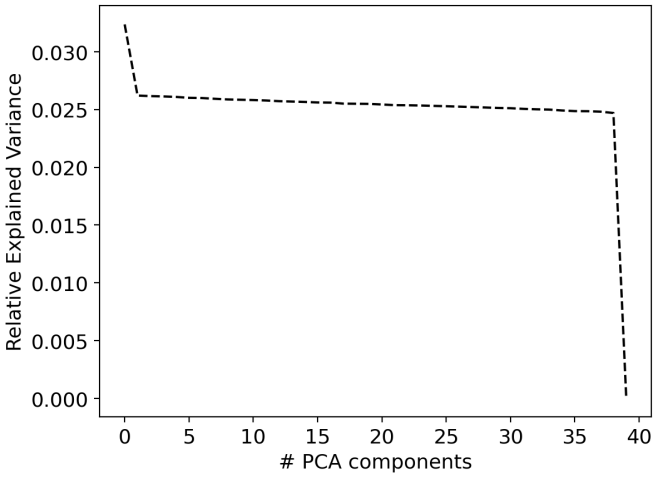

Figure 12: Relative explained variances of PCA components. Parameter fluctuation in the atom number $N = (36\,000 \pm 3600)$ at constant temperature $T = 278\,\mathrm{nK}$. Cloud expansion for early times $t_{\mathrm{TOF}} = 0.6\,\mathrm{ms}$.

to the blurring of the clouds wings at higher densities.

6.1.2 Temperature Fluctuation

Instead of a fluctuation in the atom number we now consider fluctuations in the temperature, while keeping the atom number fixed. We again consider a set of 40 images. The results are shown in Figure 15a. Theoretically, the 5% variation in T has a proportional effect on T/T_{F} while only corresponding to a 2.5% change in the cloud size $R_i \propto T^{1/2}$. The fit accuracy for the plain fit is on the order 5%. The fit accuracy does not change significantly for either the mean image or the PCA reconstructed images. Different to the variation in the atom number, the principal components in Figure 15b don't display any visible structure. The relative share of explained variance is equal for all components. This implies, that the variation in the images due to the variation in T is on the same order as the variation due to noise. For the other fit-parameters, besides T/T_{F}, fit accuracy improves for the mean image compared to the plain fit. Similar to before the fit accuracy reaches the same initial level as for the plain case once all components are added. However, no improvement in accuracy is found after adding the first component.

6.1.3 Multiple Parameter Fluctuation

We now consider the simultaneous fluctuations of multiple experimental parameters: T, N, μ_x and μ_y. The sample set consists of 40 images as before. The results of the analysis are shown in Figure 16a.

Because in this case a total of four parameters fluctuate we expect the structure to be contained in more than one principal component. This can be seen indeed in both the fit accuracy results and the components displayed in Figure 16b. For the components, the first two components show visible structure an explain a relatively larger share of the variance compared to the higher order components, which are on the same order again and therefore mostly contain noise. While the shape of the visible structure is again cloud shaped (similar to the fluctuation in N) the structure

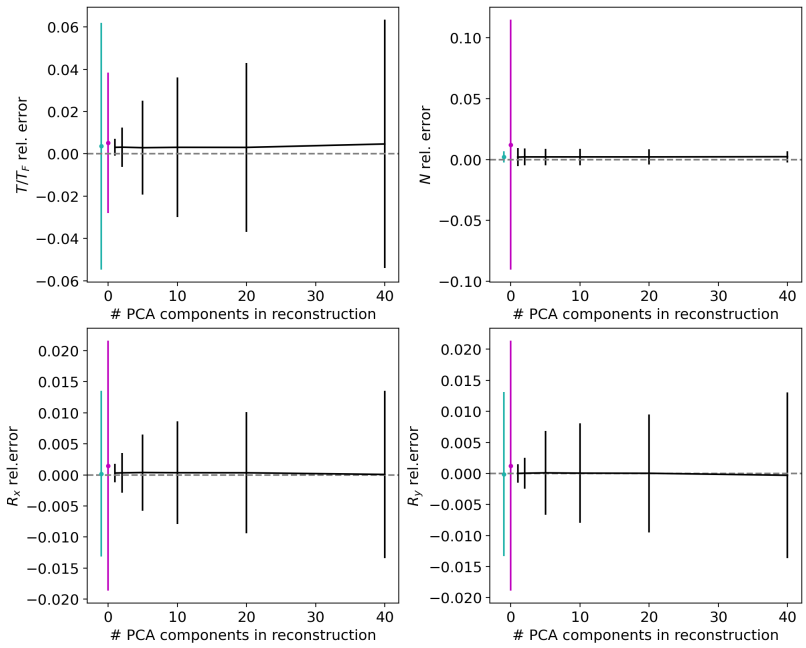

(a)

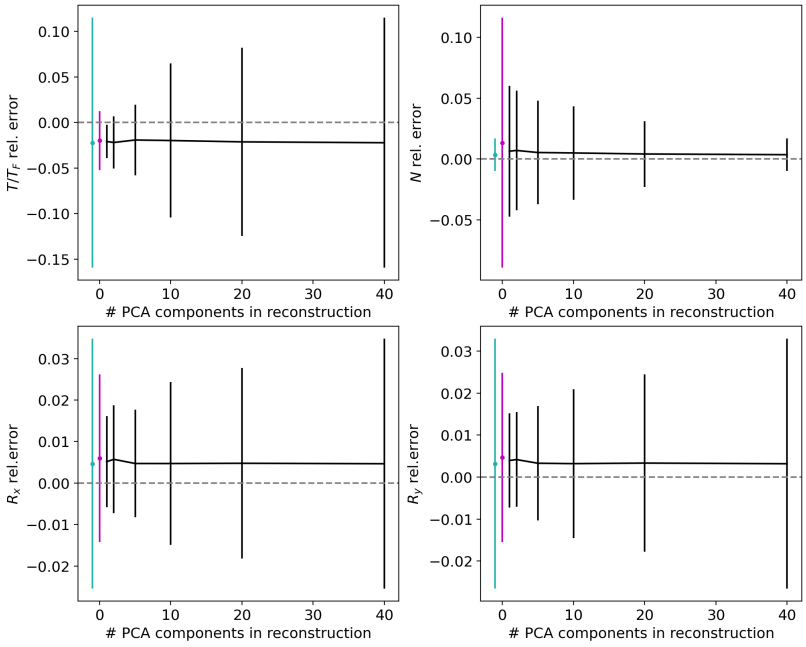

(b)

Figure 13: PCA fit accuracy results. Parameter fluctuation in the atom number $N = (36\,000 \pm 3600)$ at constant temperature $T = 278\,\mathrm{nK}$: $T/T_\mathrm{F} = (0.20 \pm 0.01)$. Cloud expansion for (a) early times $t_\mathrm{TOF} = 0.6\,\mathrm{ms}$, $R_x = (207 \pm 4)\,\mu\mathrm{m}$, $R_y = (25 \pm 1)\,\mu\mathrm{m}$ and (b) late times $t_\mathrm{TOF} = 2.1\,\mathrm{ms}$, $R_x = (223 \pm 4)\,\mu\mathrm{m}$, $R_y = (87 \pm 2)\,\mu\mathrm{m}$. —: fit accuracy of the original images, —: fit accuracy of the mean image.

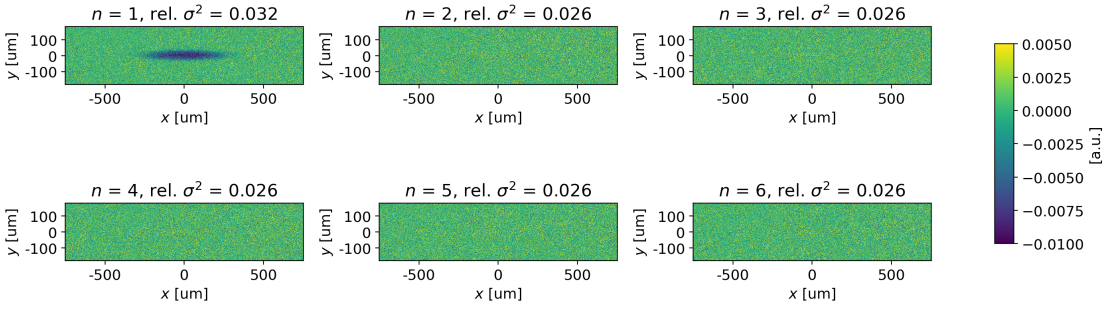

(a)

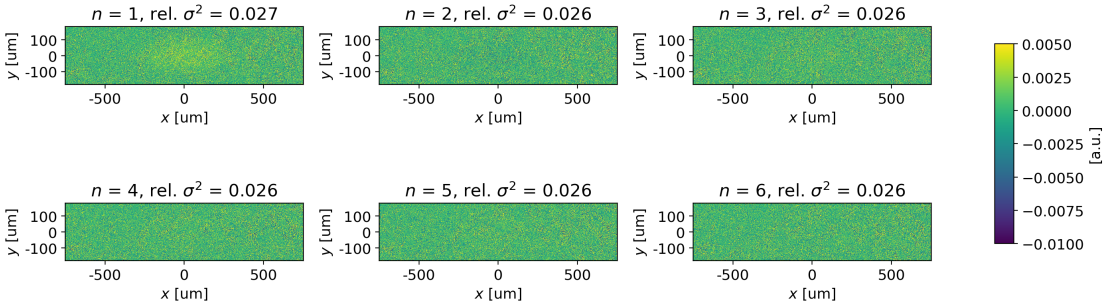

(b)

Figure 14: PCA components $n = 1 - 6$. Parameter fluctuation in the atom number $N = (36\,000 \pm 3600)$ at constant temperature $T = 278\,\mathrm{nK}$. Cloud expansion for (a) early times $t_{\mathrm{TOF}} = 0.6\,\mathrm{ms}$ and (b) late times $t_{\mathrm{TOF}} = 2.1\,\mathrm{ms}$.

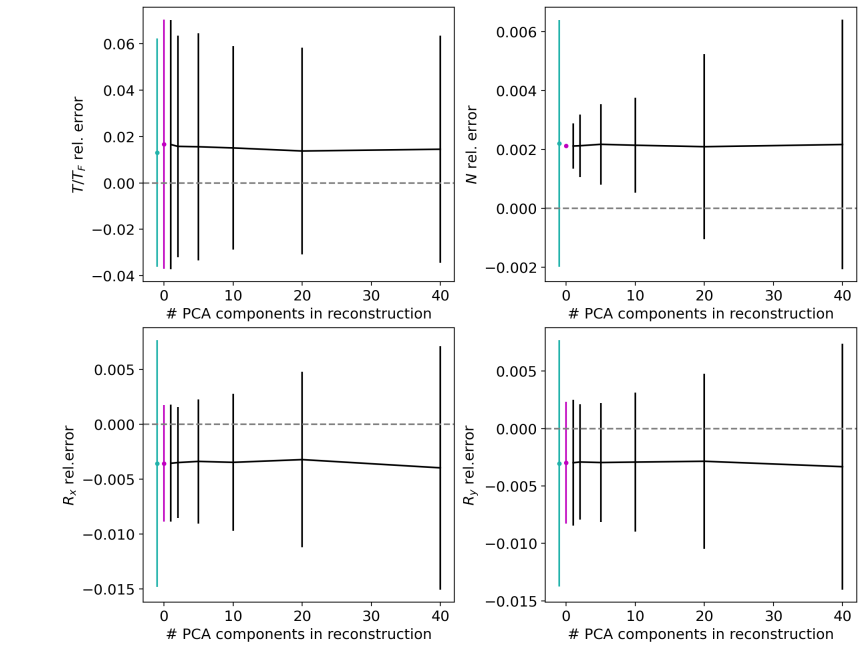

(a)

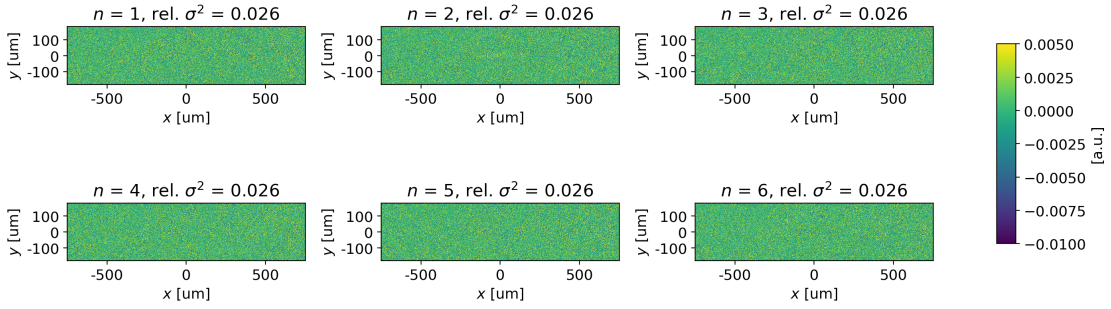

(b)

Figure 15: PCA fit accuracy results (a) and components $n = 1 - 6$ (b) Parameter fluctuation in the temperature $T = (278.0 \pm 13.9)\,\mathrm{nK}$ at constant atom number $N = 36\,000$: $T/T_\mathrm{F} = (0.20 \pm 0.02)$. Cloud expansion for early times $t_\mathrm{TOF} = 0.6\,\mathrm{ms}$, $R_x = (206 \pm 1)\,\mu\mathrm{m}$, $R_y = 25\,\mu\mathrm{m}$. —: fit accuracy of the original images, —: fit accuracy of the mean image.

looks distinctly different, splitting into an upper and lower part. This can be understood from the variation in μ_y. In the short direction $R_y \approx 25\,\mu\mathrm{m}$ a change in $2\,\mu\mathrm{m}$ is significant, while in the long direction $R_x \approx 224\,\mu\mathrm{m}$ the change in the position centre is not picked up. From the four fluctuating parameters only two, N and μ_y, are distinguished by the PCA.

For the fit accuracy this results in the highest accuracy for taking into account the first two principal components. The reconstruction with only the first parameter taken into account instead has a similar accuracy compared to the mean image. Overall the accuracy decreases compared to the fluctuation of individual parameters.

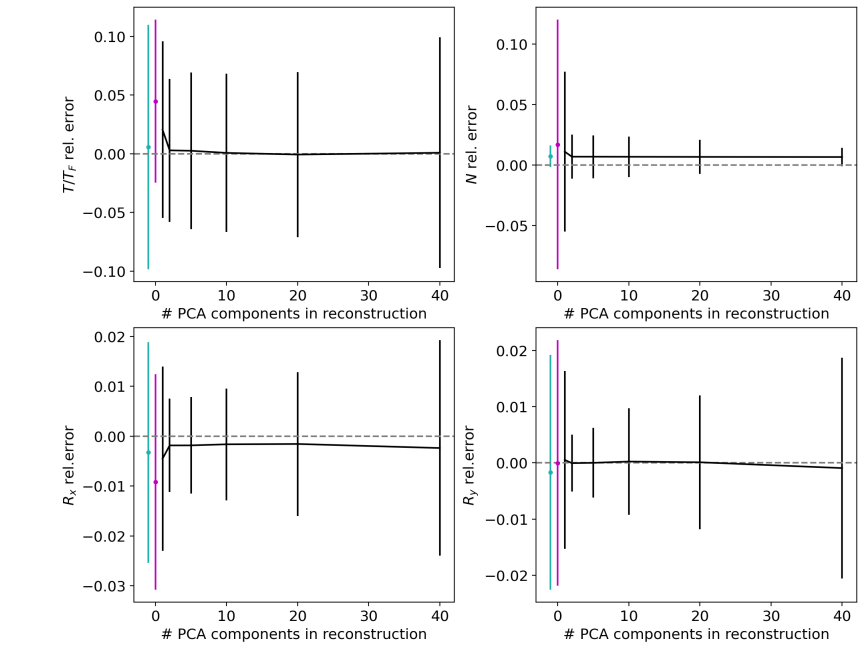

(a)

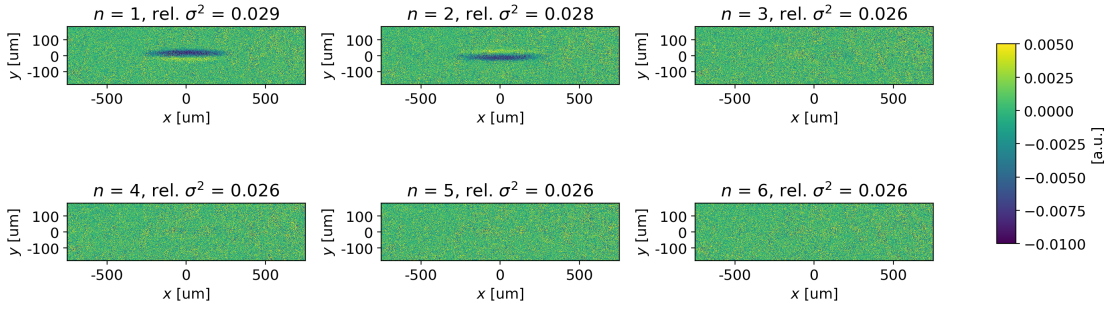

(b)

Figure 16: PCA fit accuracy results (a) and components $n = 1 - 6$ (b) Parameter fluctuation in the temperature $T = (278.0 \pm 13.9)\,\mathrm{nK}$, atom number $N = (36\,000 \pm 3600)$ and atom centre $\mu_x = (2 \pm 2)\,\mu\mathrm{m}$, $\mu_y = (2 \pm 2)\,\mu\mathrm{m}$: $T/T_\mathrm{F} = (0.20 \pm 0.02)$. Cloud expansion for early times $t_\mathrm{TOF} = 0.6\,\mathrm{ms}$, $R_x = (208 \pm 4)\,\mu\mathrm{m}$, $R_y = (25 \pm 1)\,\mu\mathrm{m}$. —: fit accuracy of the original images, —: fit accuracy of the mean image.

6.1.4 TOF Variation

Before we considered the effect of fluctuations in experimental parameters for single time instances. We now assess the effect of the PCA on a complete set of TOF images, where the experimental parameters are kept constant. The results and components are shown in Figure 17. For all components the fit accuracy is significantly degraded compared to the plain fit. Again, most of the visible structure is present in the first few components, with all higher order components explaining equal amounts of variation. Therefore, a lot of the variation due to experimental parameters, i.e. t_TOF, is not distinguished from the uncorrelated camera noise. Only once the

complete variance is added back to the image the fit accuracy is comparable with the one for the initial images. Note, that our analysis did not assess the effect on different time regimes or consider whether the temperature fit by TOF is improved. Although, the latter appears unlikely considering the error introduced in the cloud size parameters.

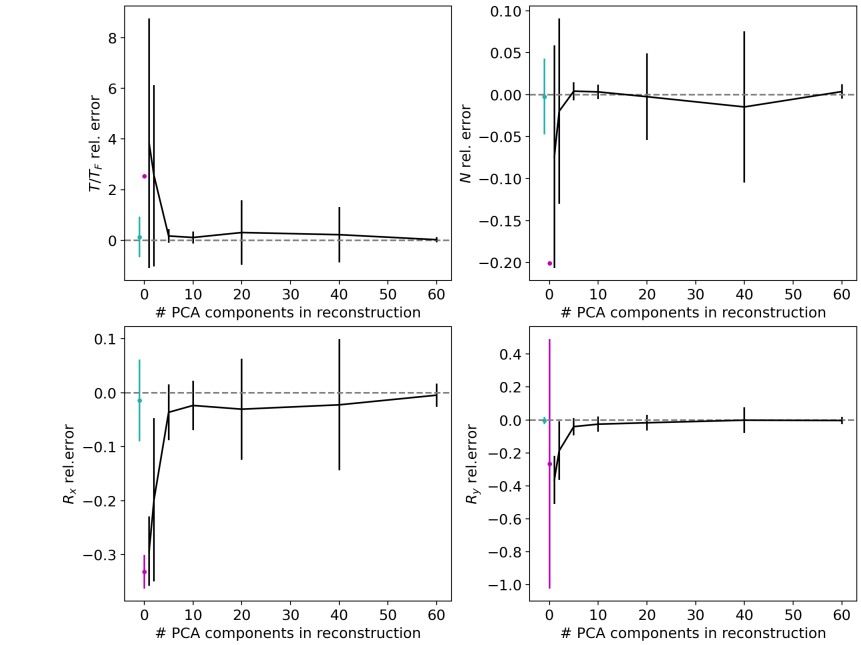

(a)

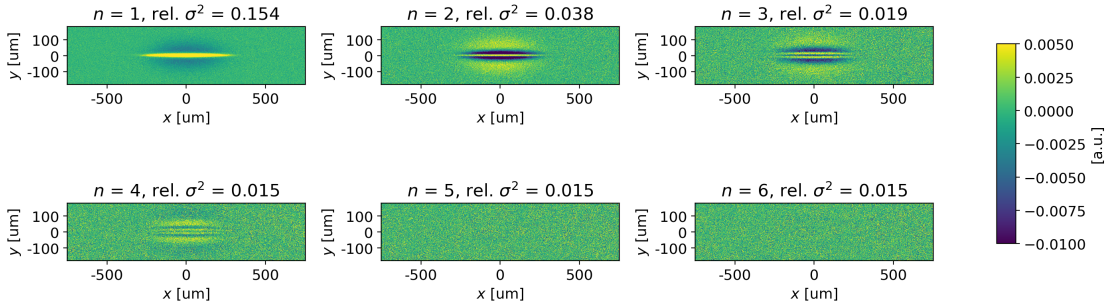

(b)

Figure 17: PCA fit accuracy results (a) and components $n = 1 - 6$ (b). TOF expansion for $t = 0.2\,\text{ms} - 2.9\,\text{ms}$: temperature $T = 278\,\text{nK}$, atom number $N = 36\,000$ and $T/T_\text{F} = 0.20$. —: fit accuracy of the original images, —: fit accuracy of the mean image.

While the results above suggest improvements in the fit accuracy for single time instance images when applying the PCA, we won't employ the PCA in the further analysis. This is due to the fact, that we don't introduce a variation in the experimental parameters. In this case performing a PCA on a set of images is equivalent to calculating an average image. As we expect the experimental parameters to fluctuate in the actual experiment involving a PCA in the data analysis of the experimental images appears advantageous, especially considering that the fit results did not degrade for the cases considered above. Looking at the principal components themselves also

provides a qualitative measure to understand whether fluctuations in the experimental data is dominated by correlated or uncorrelated noise. The analysis of results for the case of multiple fluctuating parameters indicates, however, that attributing variations in experimental parameters to single principal components is not feasible.

6.2 Influence of Imaging Noise on Fit-Parameter Accuracy

In this section we investigate the question of the fit parameter accuracy. The simulations were set up as discussed in Chapter 5.1 and run for parameter ranges as discussed in Chapter 5.2. If not stated otherwise the simulations were performed with the noise (Chapter 4.2) and imaging light profiles (Chapter 3.3) obtained directly from the experimental data. The fitting routine and data analysis follows Chapter 5. While we only present some of the fit results in this section, we provide the full set of data in Appendix E. The goal is to estimate the fit accuracy for the given set-up for the range $T/T_\mathrm{F} \in [0, 1]$. Given the influence of the peak density on the results for a sweep of the T/T_F parameter the peak density is held constant. We will first consider the fit accuracy of single images, before moving to evaluating the fit accuracy in TOF expansions.

6.2.1 T/T_F at Single Time Instance

To quantify the fit accuracy for single images we create for a given $n_{\mathrm{2D}0}$ 20 images for each T/T_F. The T/T_F values are given in steps of 0.1 in the range $[0.1, 1]$. From theses images we extract the fit parameters with the fitting routine described in 5.3. The accuracy of the fit parameter is then quantified by comparing the mean and standard deviation across the set of 20 images to the respective input parameter. We want to consider the accuracy of T/T_F and N. While these parameters are not directly obtained from the fit parameters they can be calculated from appropriate relations, as described in 5.3. The accuracy in the calculated quantity is then again determined from their mean and standard deviation. In Figure 18 the results for T/T_F of the T/T_F sweep at constant peak density $n_{\mathrm{2D}0} = 2.62 \times 10^{12}\,\mathrm{m}^{-2}$ for the Andor and $n_{\mathrm{2D}0} = 4.03 \times 10^{12}\,\mathrm{m}^{-2}$ for the Ximea are shown. For both cameras the fit accuracy decreases as $T/T_\mathrm{F} \to 1$. This is expected, as the information about the parameter is mostly contained in the wings of the density distribution. As the distribution approaches the Gaussian distribution in this limit the wings become indistinguishable for different T/T_F. In the other limit we expect the fit accuracy to decrease for T/T_F as well, as the spatial scale of the density decay falls below the pixel resolution. For the sweeps presented the degradation of the fit accuracy in the low temperature limit is less pronounced compared to the large temperature limit. Apparently, the resolution limit for low temperatures is not yet relevant at the lower bound of the sweep range $T/T_\mathrm{F} = 0.1$.

To estimate the error in the T/T_F fit parameter for the experimental parameter at $T/T_\mathrm{F} = 0.18$ we consider the data point at $T/T_\mathrm{F} = 0.2$. The fit result for the cameras are

$$\text{Ximea:} \quad T/T_\mathrm{F} = (0.18 \pm 0.16) \tag{62}$$

$$\text{Andor:} \quad T/T_\mathrm{F} = (0.200 \pm 0.014) \tag{63}$$

It is evident that for these given parameters the image of the Andor camera provides more accurate fit results. This pattern holds true for the whole range of T/T_F values.

This difference in fit accuracy is significantly reduced for increased light intensities. In Figure 19 the results for three different simulated light sources are shown. The sweep fit already improves

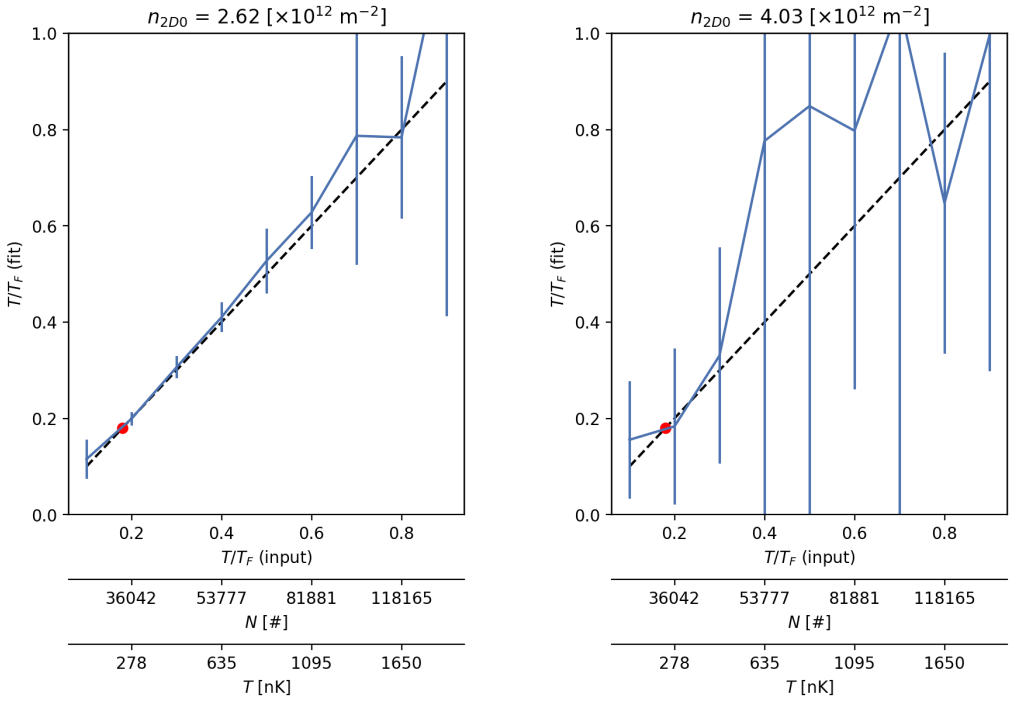

(a) (b)

Figure 18: Comparison of T/T_F fit accuracy results for a T/T_F sweep at constant peak density. (a) Andor $n_{2\mathrm{D}0} = 2.62 \times 10^{12}\,\mathrm{m}^{-2}$. (b) Ximea $n_{2\mathrm{D}0} = 4.03 \times 10^{12}\,\mathrm{m}^{-2}$. • indicates the parameter as originally obtained from the experiment.

for the case of the flat-field light source, compared to the light source with fringes. If instead a light source at higher intensity $0.075 I_\mathrm{sat}$, but including fringes is used, the fit accuracy improves significantly.

Due to the Beer-Lambert relation for the absorption we expect the signal to strongly depend on the density of the cloud. In Figure 20 the fit results are displayed for different peak densities. In the case of the Ximea the fit results become meaningless for peak densities less than $n_{2\mathrm{D}0} = 4 \times 10^{12}\,\mathrm{m}^{-2}$ and $OD_{2\mathrm{D}0} \approx 0.2$. Most fitting routines don't converge or the results have large uncertainties attached to them. In the case of the Andor the fit accuracy degrades for lower peak densities as well, but is able to resolve T/T_F for lower densities than the Ximea. Even at $n_{2\mathrm{D}0} = 0.65 \times 10^{12}\,\mathrm{m}^{-2}$, $OD = 0.14$ the T/T_F can be resolved in the mean, even if the uncertainty increases to $\Delta T/T_\mathrm{F} = 0.17$ At peak densities higher than $n_{2\mathrm{D}0} = 2.62 \times 10^{12}\,\mathrm{m}^{-2}$, $OD = 0.68$ the T/T_F fit accuracy improves for T/T_F in the range 0.2 - 0.7. For larger T/T_F the fit accuracy continues to have a similar uncertainty attached. The largest optical considered during this simulation run is $OD = 1.12$. At this level the fit accuracy for $T/T_\mathrm{F} = 0.1$ degrades to $T/T_\mathrm{F} = 0.15(5)$. The data can be found in Appendix E. We did not probe higher optical densities at which saturation effects become significant.

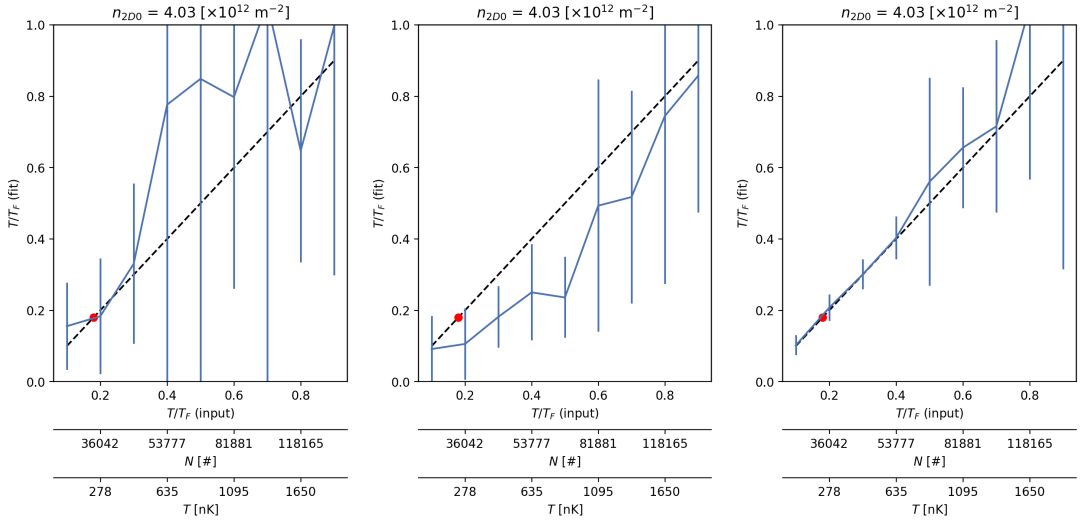

(a) (b) (c)

Figure 19: T/T_F fit accuracy results for T/T_F sweep at constant peak density $n_{2\mathrm{D}0} = 4.03 \times 10^{12}\,\mathrm{m}^{-1}$ for different simulated light sources with the Ximea: (a) $I = 0.0049 I_\mathrm{sat}$ (fringes), (b) $I = 0.0049 I_\mathrm{sat}$ (flat-field), (c) $I = 0.075 I_\mathrm{sat}$ (fringes), $t_\mathrm{pulse} = 3\,\mu\mathrm{s}$. • indicates the parameter as originally obtained from the experiment.

6.2.2 Atom Number at Single Time Instance

Following T/T_F we now consider the accuracy of N as determined from the fit parameters by Equation (17). The results are shown in Figure 21. We again estimate the uncertainty for the original experimental value by looking at the $T/T_\mathrm{F} = 0.2$ data point.

$$\text{Ximea:} \quad N = (35\,800 \pm 2200) \tag{64}$$

$$\text{Andor:} \quad N = (36\,300 \pm 300) \tag{65}$$

While the results are still worse for the Ximea, compared to the Andor, in both cases the relative uncertainty in the fit parameter is far lower than the relative uncertainty in the case of T/T_F. It turns out that this result holds true for broad ranges of peak densities and T/T_F values. Remarkably, even if the fit accuracy is low across all cloud parameters (R_x, R_y $n_{2\mathrm{D}0}$ and T/T_F), the atom number appears to be reliable. As an example we present the fit parameters at low peak density and calculated atom number in Figure 22. It appears that the fit parameter adjust such that the overall atom number is conserved. This phenomenon can be explained, by considering the definition of the atom number in Equation (6). The atom number is an integrated quantity, which does not depend on the local make-up of the cloud, but only the global total absorption. This leads to a low susceptibility to noise of the atom number and makes it a very reliable quantity.

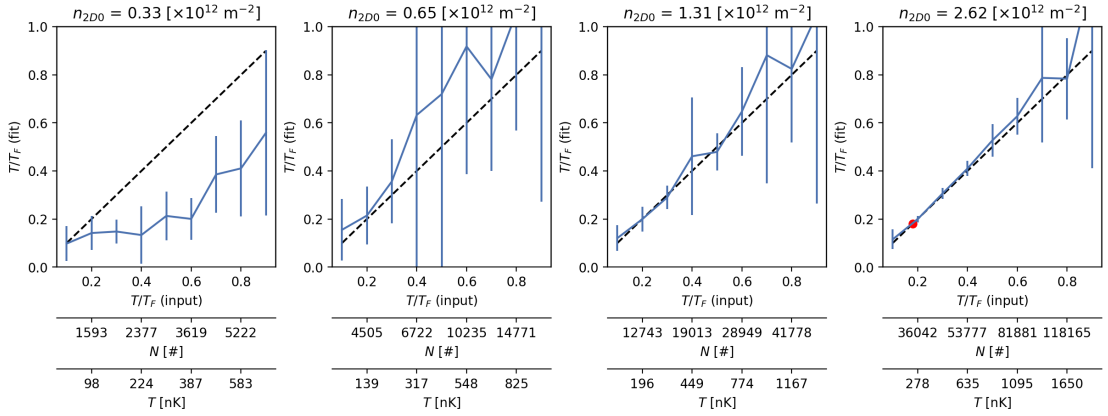

(a)

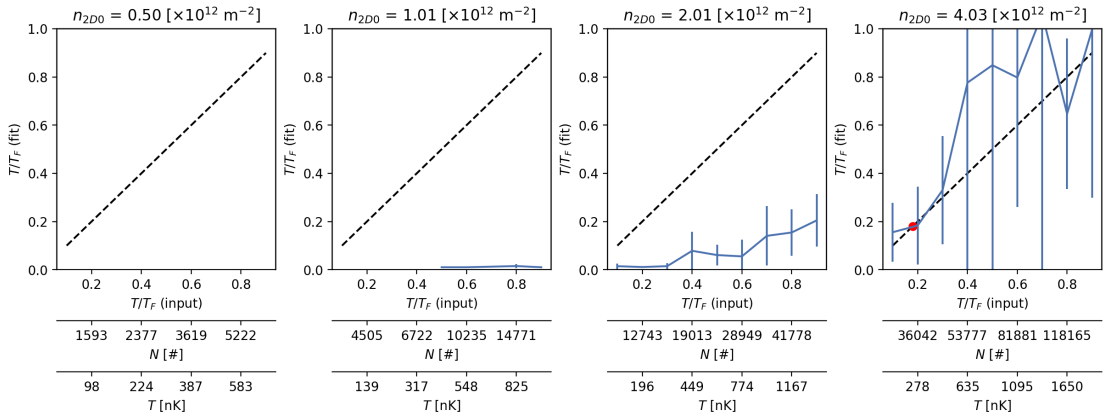

(b)

Figure 20: T/T_F fit accuracy for a T/T_F sweep of different constant peak densities (increasing left to right). The fit parameters are determined for the Andor (a) and Ximea (b) camera. The absence of data points indicates lack of convergence of the fit. • : indicates the parameter as originally determined from the experiment.

6.2.3 TOF

After the discussion of the fit accuracy at single time instances we now discuss the fit accuracy for time-of-flight expansion cloud images, as discussed in 2.3. Here we consider time of flight expansions from 0.2 ms to 2.9 ms. A set of 5 images is created for each of the 12 time steps spanning the time interval. For the two parameters we discuss, T and T/T_F, the accuracy for a given T/T_F and peak density n_{2D0} is then determined from the TOF analysis of the time series consisting of 60 images. Due to the low fit accuracy of the Ximea, as discussed above, we only discuss the Andor camera in this part of the analysis. Because at higher light intensities the Ximea appears to provide a comparable fit accuracy as the Andor it might be assumed that the results for the TOF parameter accuracy of the Andor will be qualitatively similar in the high intensity regime of the Ximea.

The TOF is usually performed to obtain a temperature measurement of the cloud. By addition-

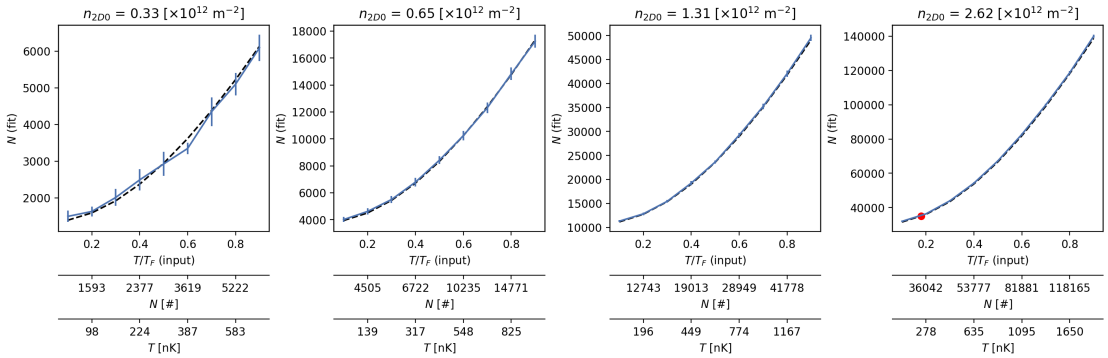

(a)

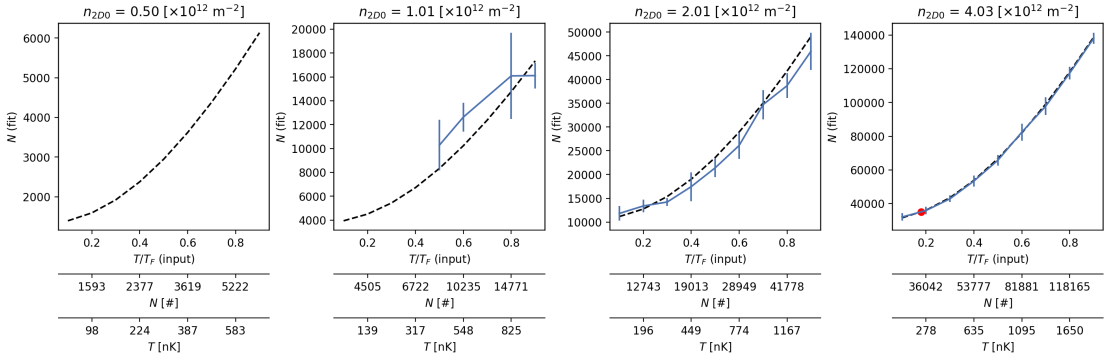

(b)

Figure 21: Atom number fit accuracy for a T/T_F sweep of different constant peak densities (increasing left to right). The fit parameters are determined for the Andor (a) and Ximea (b) camera. The absence of data points indicates lack of convergence of the fit. • : indicates the parameter as originally determined from the experiment.

ally estimating the atom number from the fit parameter the T/T_F parameter can be deduced as well (cf. Equation (12)). Because the scaling of the Gaussian cloud size is the same as the Fermi cloud size, both can be used to obtain the temperature estimate. We will discuss both methods in the following. The results for the temperature measurement in the long (x) and short (y) direction are shown in Figures 24a and 24b, respectively. The T/T_F estimate is shown in Figure 24c.

For the temperature T as obtained from the fit in the long and short direction, we observe that the temperature is more accurately determined in the short direction across the whole range of T/T_F. While for $T/T_\mathrm{F} < 0.3$ the temperature we obtain from the Fermi cloud size does not differ substantially from the input temperature, at higher T/T_F the temperature isn't resolved any more. In both cases the Fermi fit tracks the temperature more closely for low T/T_F. In the long direction the temperature we determine from the Gaussian strictly overestimates the temperature. On the other hand, the Gaussian fit improves over the Fermi fit for $T/T_\mathrm{F} > 0.5$ for lower densities and tracks the same temperature as the Fermi fit for higher densities. Additionally, the uncertainty in the Gaussian fit is far smaller than the Fermi fit across all realizations. This is again due to the fact, that much of the temperature information is contained in the wing shape

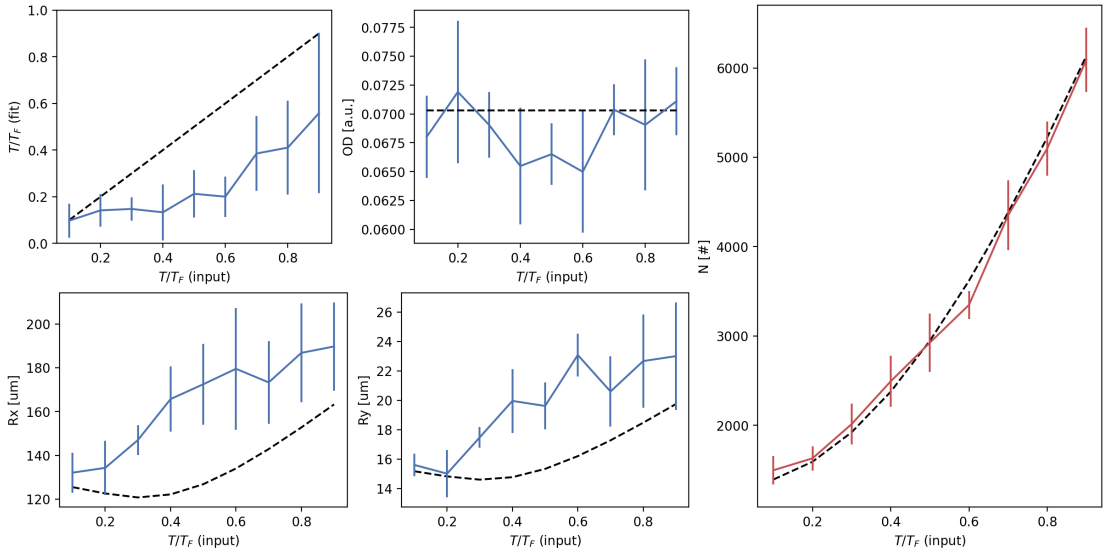

Figure 22: Fit accuracy of cloud parameters for a T/T_F sweep at constant peak density $n_{2\mathrm{D}0} = 0.33 \times 10^{12}\,\mathrm{m}^{-2}$. The fit accuracy of the calculated atom number is shown in red.

of the cloud, which the Gaussian fit does not track for lower T/T_F. In Figure 23 we give an example for a single time of flight simulation from the sweep. In this example the error in the Gaussian sizes is orders of magnitudes larger than the error in the Fermi fit. Nevertheless, the fit parameters are consistent between cloud images for the same expansion time. From the plot one can deduce that different to the Fermi fit the Gaussian fit overestimates the size of the clouds at late times. This in turn then leads to an overestimation of the temperature.

The reason the temperature fit is more reliable in the short direction is due to the relative change in cloud size during the expansion time. If the uncertainty in the size is on the order of the change in size then the temperature fit quality deteriorates. The behaviour for low T/T_F is unexpected, as for lower temperatures the relative change in size decreases. A possible reason for this behaviour is that, as we saw in the previous section, the fit is more accurate for smaller T/T_F. The increased accuracy in the cloud size parameters appears to be more significant than the reduced change in cloud size. Different to the discussion above the density dependence is less pronounced across the density regimes, with the uncertainty in the temperatures increasing slightly for higher peak densities.

Last, we discuss the accuracy of the T/T_F parameter as shown in Figure 24c. Here we only consider the temperature estimates in the short direction, due to their greater reliability. For T/T_F, similar to the temperature case, the Gaussian fit overestimates T/T_F in the low T/T_F limit. This is expected, as the parameter is calculated by means of the atom number and temperature. As the atom number is determined very accurately by the Gaussian fit, the deviation in the temperature measurement directly propagates to the accuracy of the T/T_F parameter. The accurate determination of temperature and atom number by the Fermi fit translates to an accurate estimate of the T/T_F parameter. This estimate is complemented by T/T_F as determined from the cloud parameter directly. Here we consider the mean of the T/T_F measurement across all images of the TOF time series. This direct fit method has a similar accuracy and slightly lower uncertainty in the low T/T_F regime. In the large T/T_F regime the method becomes less

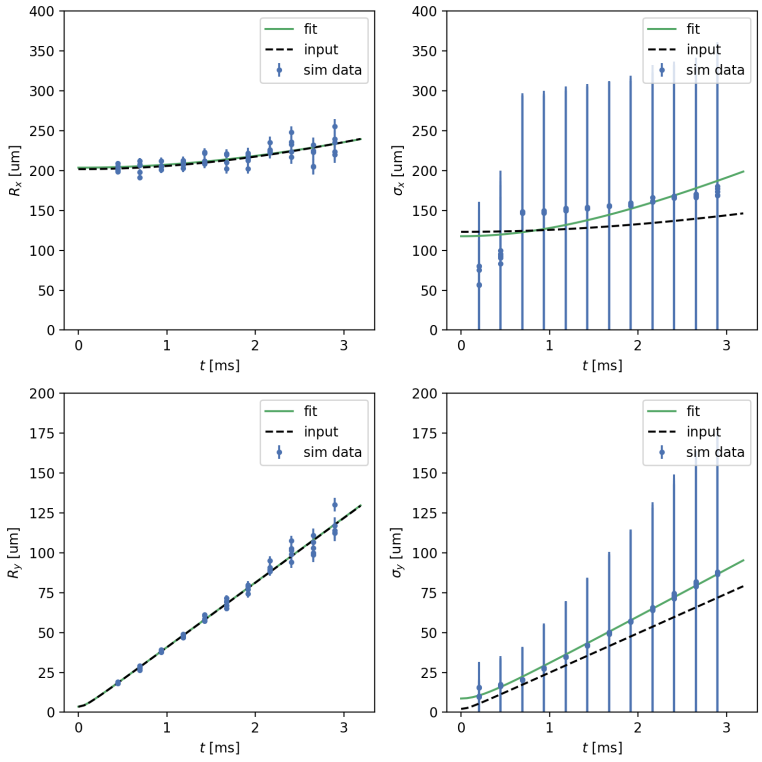

Figure 23: TOF time series and fit result: $T/T_F = 0.3$, $n_{2D0}(t = 0) = 18.7 \times 10^{12}\,\mathrm{m}^{-2}$. The cloud sizes in the long (x) direction as determined by the Fermi fit (top left) and Gaussian fit (top right) as well as the cloud sizes determined in the short (y) direction by the Fermi fit (bottom left) and Gaussian fit (bottom right). The input cloud expansion (—) and fitted cloud expansion (—) are shown as well.

accurate compared to the temperature method. It should be noted, that we do not take into account any uncertainty in the trapping frequency ω used to calculate T_F from the atom number, which would increase the uncertainty in the temperature method.

The above discussion of the fit parameter accuracy from a TOF allows for some tentative results. First, the Gaussian fit appears to become unreliable in the low T/T_F regime, wherefore a Fermi fit becomes necessary to reliably determine the temperature and T/T_F parameter. Second, both methods to determine T/T_F, from the direct fit and from the temperature and atom number appear to provide a similar accuracy.

6.3 Ramp-down Fit Reliability

After we analysed the dependence of the fit parameter accuracy for different density and T/T_F regimes, we now attempt to estimate the uncertainty in the fit parameters for a specific set of data obtained from the experiment. In the experiment a ramp-down in an optical dipole-trap was performed during which the trapping frequency ω is continuously lowered. When lowering the trap frequency fast atoms are lost such that the temperature and atom number decreases. In theory T/T_F remains constant during the procedure. In the experiment T/T_F was measured by

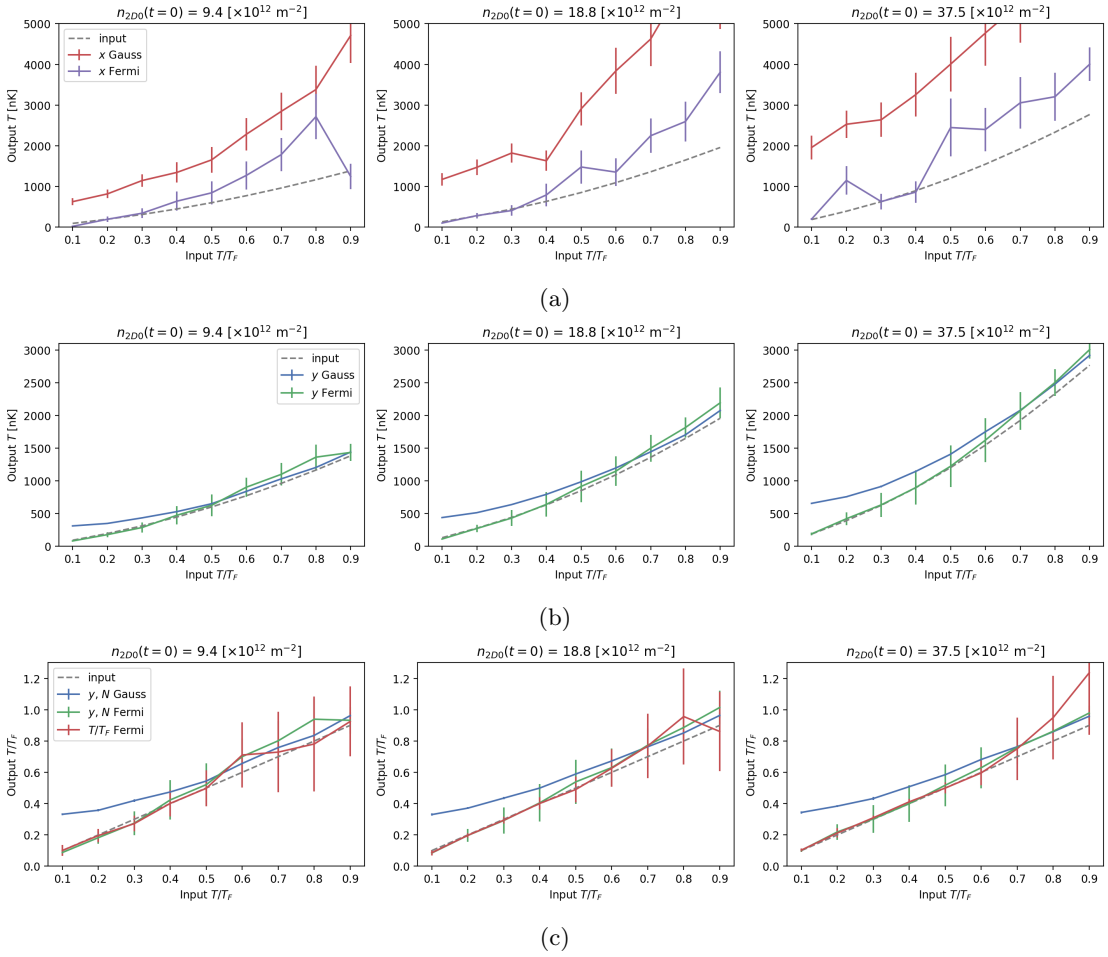

Figure 24: TOF fit results for T/T_{F} sweep of constant $n_{2\mathrm{D}0}$. (a) T fit in the long (x) direction, (b) T fit in the short (y) direction, (c) T/T_{F} fit. i, N denotes T/T_{F} estimate from T TOF fit in i-direction and mean N. T/T_{F} Fermi denotes T/T_{F} estimate from mean of all fitted T/T_{F}.

means of a TOF expansion for different values of the trapping frequencies. The T/T_F parameter can be obtained either directly from the cloud parameters or from the temperature and atom number as explained in 5.3. The experiment and analysis of the experimental data was performed by other members of the group.

To estimate the uncertainty due to camera noise we simulate a TOF expansion for the atom number N, temperature T and trap frequencies obtained from the experimental data. Here it should be noted, that the input parameter heavily bias the simulation and its result. Furthermore, because the experimental and simulated images were analysed separately, different fitting routines were used. While the same fitting function was used, the initial parameters,the chosen fitting regions and selection criteria for excluded data points might differ. Therefore, it needs to be assumed that this circumstance explains at least part of the difference between the simulated and experimental data. We simulate the TOF with the same time steps and image sample sizes as the experiment. In the case of the Andor the cloud was measured at 7 equidistant time steps from 0.1 ms to 0.7 ms with 9 images taken at each time step. In the case of the Ximea the cloud was measured at 12 equidistant time steps from 0.8 ms to 2.5 ms with 9 images taken at each time step. Note, that for these simulations we adjusted the light intensity and sensitivity to closer match the experiment as described in Appendix D. The experimental and simulation results are shown in Figure 25.

The experimentally obtained T/T_F does decrease during the ramp down. The range of T/T_F is 0.06-0.39. The range of mean trap frequencies are 2π 765 Hz to 2π 3014 Hz, all above the frequency $\omega = 2\pi$ 483 Hz considered in the previous sections. In all cases the simulated T/T_F, both for the direct and expansion method agree with the input parameter within their uncertainty. This is consistent with the results of the previous sections. The T/T_F estimate for the experimental by the direct method is on average 58% lower than estimated by the expansion method for the Andor data. The simulation does not reproduce this behaviour. Instead, the T/T_F estimation from the simulated data by the direct method closely tracks the input parameter from the expansion method. This discrepancy in the experimental data can therefore not be accounted for by noise in the imaging process.

For the Ximea the T/T_F estimate agrees far better for both methods which is then reproduced by the simulated data. Interestingly the uncertainty in T/T_F by the expansion method is similar for both simulation and experiment. For the direct method on the other hand the uncertainty attributed to the data points by the simulation is far lower compared to the experiment. This could indicate strong shot-to-shot fluctuations in both the temperature and atom number. The attribution of this observation is, however, not certain due to the aforementioned difference in fitting procedure. We might also make the observation, that in case of the expansion method T/T_F has a closer agreement between experiment and simulation for the Andor then the Ximea, which suggest the Andor data to be less influenced by imaging noise.

This proof-of-concept comparison of simulated and experimental data indicates a few possible paths to use the simulation to understand the uncertainty attached to experimental results. First, we can estimate whether a discrepancy between values can be accounted for by noise in the imaging process. Second, if data points match we can compare uncertainties to estimate the uncertainty in the experimental data point not explained by imaging noise but fluctuations in the experimental parameter. For this it is necessary, however, to use the exact same fitting routine for both analyses. Third, if simulation and experiment disagree significantly this can indicate, that in the regime of interest the accuracy of the experimentally obtained fit parameters is lower than assumed. This method is, however, not suited to verify single data points in any case.

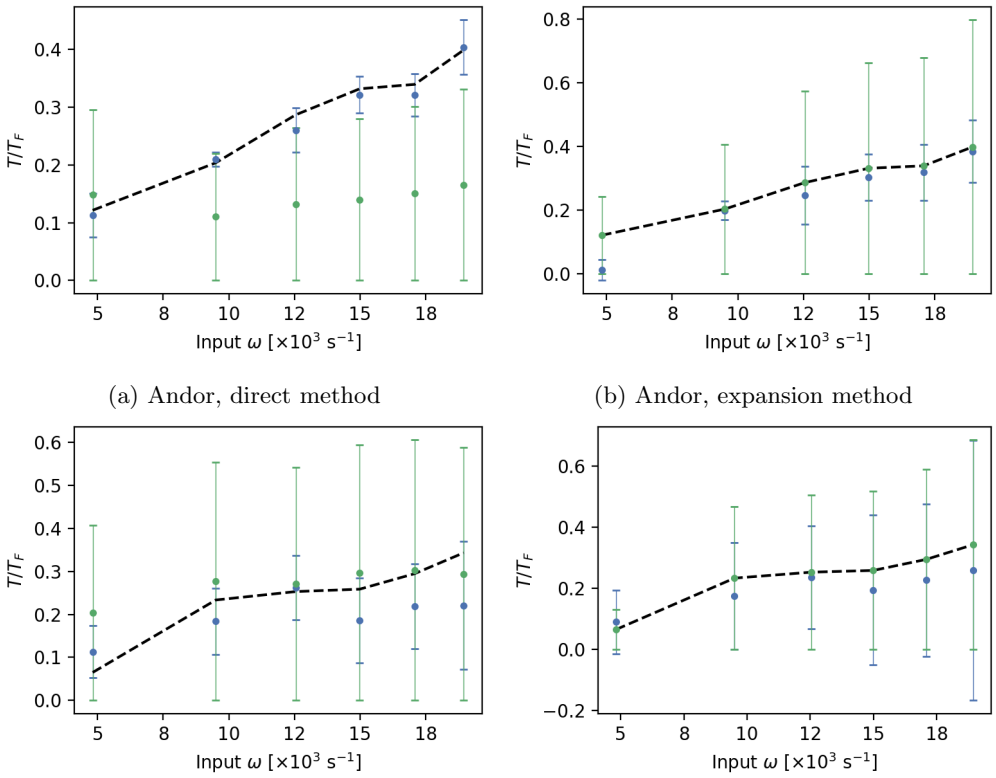

(a) Andor, direct method

(b) Andor, expansion method

(c) Ximea, direct method

(d) Ximea, expansion method

Figure 25: Experimental (—) and simulation (—) results for the T/T_F parameter of a ramp-down in an optical dipole-trap measured by a time-of-flight expansion. The simulation input parameters (—) N and T are determined by the fit parameters of the experimental data. The input parameter of the mean trap frequency ω is determined from an independent measurement. The direct method correspond to the calculation of T/T_F directly from the cloud parameters. The expansion method calculates T/T_F by means of the temperature of the TOF, the atom number and mean trap frequency.

7 Conclusion and Outlook

In this thesis we constructed a numerical simulation of the absorption imaging process of an ultracold ^{6}Li cloud to estimate the effect of camera noise and the light source on the fit accuracy of the cloud parameters. The camera noise was modelled by considering different sources of noise present in CCD cameras and determining their relevance. The noise model was then calibrated with the noise found in images taken from the experiment. The spatial intensity distribution for the light source was similarly characterized by considering images taken from the experiment and calculating the intensity from given camera parameters. In the case of the Ximea this yielded an unexpectedly low intensity, for which since additional measurements by a photo-diode have been performed showing the incident intensity to be larger than estimated from the camera (for a discussion confer Appendix D). The intensity results for the Andor, however, still hold as presented in the thesis.

For the absorption images we modelled the absorption process and cloud density distribution for appropriate parameters obtained from the experiment. To extract the cloud parameter we implemented a fitting routine such that we could fit both Fermi and Gaussian density profiles. The accuracy of an image fit can then be determined by comparing the input parameters of the cloud with the extracted parameters.

We found that for densities realised in the experiment, the accuracy in the fit parameter as determined from a harmonically trapped Fermi gas distribution improves for low T/T_F, theoretically allowing to distinguish T/T_F up to $\Delta T/T_\mathrm{F} = 0.02$ in the regime $T/T_\mathrm{F} < 0.3$ using the Andor camera. We showed that the Ximea has difficulty to resolve the clouds at the light intensity determined from the experimental images. At higher intensities the fit accuracy improves significantly for the Ximea. Due to the issues involved with the intensity measurement, a precise accuracy estimation still needs to be worked out. We further showed that for both cameras the atom number is reliably determined from the fit parameters, even in the low density and low intensity regimes.

By simulating image series of time-of-flight expansion we could show that the temperature as estimated from the cloud size expansion by a Gaussian fit systematically overestimate the temperature in the low T/T_F regime. In this regime only by considering the cloud size of the Fermi cloud distribution we can reliably measure the temperature. For the estimation of T/T_F we examined two methods. In one method the parameter is determined directly from the cloud parameters. In the other the parameter is calculated from the temperature determined from the time-of-flight expansion, the average atom number and trap frequency. We showed that both methods are equally accurate.

We extended the above analysis of the fit accuracy to a particular set of experimental data points obtained by TOF measurements of a ramp-down sequence. We simulated these TOF image series with the input parameters given by the fit parameters of the experimental images. While this analysis cannot verify the experimental results, it proved insights into the uncertainty explainable by camera noise compared to fluctuations in the experimental parameters. It thereby can help to analyse whether the discrepancy between two experimentally obtained data points can be explained by camera noise alone.

Last, we assessed the feasibility of using a principal component analysis to distinguish correlated noise in the images due to fluctuations in the experimental parameters from uncorrelated noise introduced by the imaging process. We showed that using the principal component analysis fit results improved significantly. Furthermore, the principal components can be used to gain a qualitative understanding of the relative magnitude of fluctuations in the experimental

parameters.

While the simulation does not capture all noise and fluctuations associated with the imaging of cold atomic clouds it can provide of the resolvability of cloud parameters in different density and temperature regimes. Moreover, due to the high level of control it is well suited to evaluate other data analysis and noise reduction techniques.

Appendix

Appendix A Camera Parameters

In Table 1 we summarize relevant camera parameters referred to in this thesis.

Table 1: Summary of camera parameters.

Property	Andor iKon-M	Ximea xiD
Model	DU934P-BEX2-DD-9OT	MDO28xU-SY
Resolution	1024 x 1024	1934 x 1456
Pixel size [μm]	13x13	4.54x4.54
Effective pixel size [μm]	1.86x1.86	8.28x8.28
QE @ 671 nm	0.93	0.9
Read-out noise [e^-]	21.7	8.3
Dark-current noise [e^-/px/s]	0.01 ($T = -80\,°C$)	N/A ($T = 30\,°C$)
Sensitivity [e^-/ADU]	6.2	1.37

- Because the Andor camera is operated in the fast kinetics mode, images are only taken on a 1024x196 subsection of the pixel array.

Appendix B Spline Approximation of Li_s

During the simulation and fit procedure the function

$$\mathrm{Li}_2\left(-\mathrm{e}^z\right) \tag{66}$$

is called numerous times, due to its occurrence in the column density (cf. Equation (18)). The implementation, as found in the `mpmath` library is computationally expensive. Our goal is to construct a computationally less expensive approximation to this function with sufficient accuracy.

To this end we used a cubic spline interpolation as explained in [Kong et al., 2021]. The strategy is to approximate a set of n data points (x_i, y_i) with piecewise defined cubic polynomials. That is, one cubic polynomial $S_i(x) = a_i x^3 + b_i x^2 + c_i x + d_i$ defined for each of the $n-1$ intervals $[x_i, x_{i+1}]$.

The coefficient for the polynomials can be found by demanding that the splines intersect the data points at the interval boundaries

$$S_i(x_i) = y_i \tag{67}$$
$$S_i(x_{i+1}) = y_{i+1} \tag{68}$$

and that the first and second derivative be continuous

$$S_i'(x_{i+1}) = S_{i+1}'(x_{i+1}) \tag{69}$$
$$S_i''(x_{i+1}) = S_{i+1}''(x_{i+1}). \tag{70}$$

Additionally, two boundary constraints are required. Usually, the second derivative at the end points is set to zero.

$$S_1''(x_1) = 0, \quad S_{n-1}''(x_n) = 0 \tag{71}$$

The effect of this choice will be discussed again.

Ton construct the spline we used the `scipy.interpolate.CubicSpline` module, which implements the computation of the spline coefficients.

The data points in our case are a sample of 66, where we consider the implementation from the `mpmath` library as the ground truth.

The region of interest for the parameter z is derived from the expression for z in Equation (18)

$$z = q - \left(\frac{x^2}{2R_x^2} + \frac{y^2}{2R_y^2}\right) f(\mathrm{e}^q) \tag{72}$$

We assume the following bounds for the parameters

$$T/T_\mathrm{F} \in [0.002, 6] \rightarrow \begin{cases} q & \in [500, -7] \\ f(\mathrm{e}^q) & \in [500, 1] \end{cases} \tag{73}$$

$$\left.\begin{matrix} x, y \in [0\,\mu\mathrm{m}, 8000\,\mu\mathrm{m}] \\ R_x, R_y \in [1\,\mu\mathrm{m}, 8000\,\mu\mathrm{m}] \end{matrix}\right\} \rightarrow \left(\frac{x^2}{2R_x^2} + \frac{y^2}{2R_y^2}\right) \in [0, 6.4 \times 10^7] \tag{74}$$

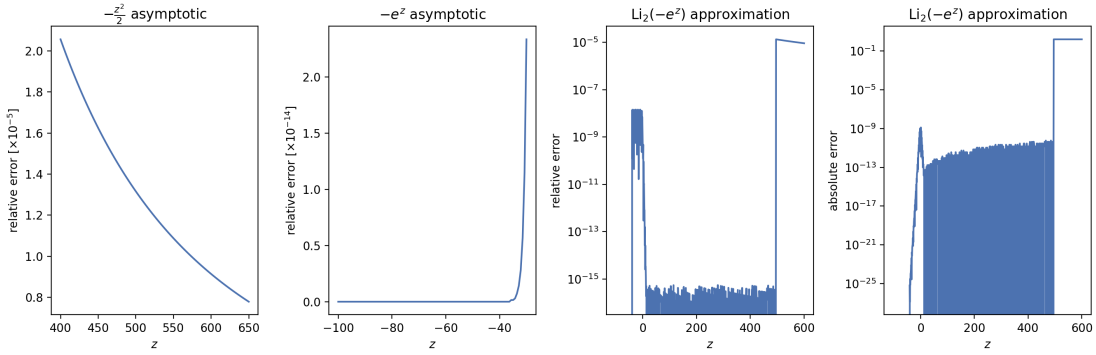

Figure 26: Deviation of the asymptotic approximations and spline approximations from the function $\mathrm{Li}_2(-\mathrm{e}^q)$.

which yields

$$z \in [-3.2 \times 10^{10}, 500] \tag{75}$$

Where the upper limit is determined by the lower bound of T/T_F. The limits in x, y are given by the effective size of the CCD array and the lower limit of the cloud size is determined by the minimum effective pixel size.

The asymptotics of the function are

$$\mathrm{Li}_2(-e^z) = \begin{cases} -e^z & \text{for } z \to -\infty \\ -\frac{z^2}{2} & \text{for } z \to \infty \end{cases} \tag{76}$$

Their relative error is shown in Figure 26 for $z < -30$ and $z > 400$. In the case of large negative value the asymptotics the relative deviation from the function is less than 10^{-5}. Whereas for large positive values the asymptotic deviates more $\lesssim 2 \times 10^{-5}$. Note that $z > 400$ corresponds to $T/T_\mathrm{F} < 0.0025$, a regime we are unlikely to enter.

We can therefore extend our interpolated functions to all values $z \in (-\infty, \infty)$ by substituting the asymptotics for large arguments.

$$g(z) = \begin{cases} -\exp(z) & z < -40 \\ \mathrm{CubicSpline}(z) & -40 \leq z \leq 500 \\ -z^2/2 & z > 500 \end{cases} \tag{77}$$

The region considered for the cubic spline interpolation is then restricted to

$$z \in [-45, 505] \tag{78}$$

which we partition in 4000 equidistant intervals. We purposefully extended beyond the asymptotic boundaries, such that the boundary conditions of the spline do not concern us. The relative and absolute deviation from the actual function are displayed in Figure 26. For $z < 480$ the relative error remains below 10^{-8} with an absolute deviation no larger than 10^{-9}. We estimate

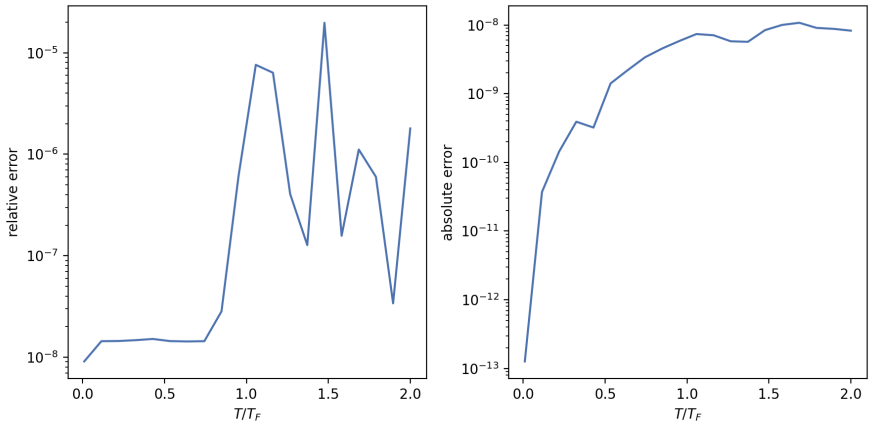

Figure 27: Maximal relative and absolute deviation from the actual function value of (79) for the CubicSpline implementation on the Ximea effective pixel grid for $R_x = R_y = 50\,\mu\mathrm{m}$ and $T/T_\mathrm{F} \in [0.01, 2]$.

the speed-up by measuring the time of seven evaluations of the function on 10^6 values on the interval $[-100, 200]$.

`mpmath`:	$(12.1 \pm 0.2)\,\mathrm{s}$
CubicSpline+Asymptotics:	$(36.1 \pm 0.8)\,\mathrm{ms}$

a speed-up of about 300 times.

In the actual expression of the column density we compute the fraction

$$\frac{\mathrm{Li}_2\left(-\exp\left[q - \left(\frac{x^2}{2R_x^2} + \frac{y^2}{2R_y^2}\right) f(e^q)\right]\right)}{\mathrm{Li}_2(-e^q)} \tag{79}$$

We calculate the relative and absolute deviation on the Ximea camera grid for R_x, R_y and variable $T/T_\mathrm{F} \in [0.01, 2]$. The results are shown in Figure 27 The results show that while the relative is low for all T/T_F with a relative error below 10^{-6}, the lowest deviations are found for low T/T_F.

Therefore, we can replace the mpmath implementation with the approximate function g.

Appendix C Pixel Density Average

The intensity at point x, y in the object plane is given by (32). As the pixel size is finite, the intensity incident on a pixel is not equal to the intensity at the centre of the pixel. In the following we will discuss this effect and our implementation in the simulation. In this analysis we don't consider variations of intensity across the image. Due to the form of (32) we expect the deviation to be most significant if the variation across the pixel is large. In regimes of small optical density $OD = \sigma_0 n \ll 1$ it is equally possible to average the density instead and calculate the transmission for this average density.

To analyse this behaviour, we again consider a cloud with parameters $T = 278\,\mathrm{nK}$, $N = 36000$ and optical trap frequencies as described in 5.2. Additionally, we apply an offset of $mu_x = 1\,\mu\mathrm{m}$, to see how the asymmetry of the cloud with respect to the pixel grid changes the results. The cloud density is considered at in-situ and after an expansion time of $t = 0.6\,\mathrm{ms}$. The column density is of course different for the two camera set-ups. We calculate an average column density value of each pixel by averaging the column density in the short-direction (x) across the length of a single pixel. The results are shown in Figure 28. In the Figure we additionally plot two relative errors. First, the relative error of $n_{2\mathrm{D}}$ at the pixel centre compared with the pixel average of the column density. Second, the relative error of the pixel centre and the average value across the pixel obtained from averaging the transmission, i.e.

$$\bar{n}_{2\mathrm{D}}(i,j) = \frac{-1}{\sigma_0} \log\left(\mathrm{mean}_{i,j}\left(\exp(-\sigma_0 n_{2\mathrm{D}}(x,y))\right)\right) \tag{80}$$

For both cameras the deviation of the density at the pixel centre from the average pixel density is largest in the wings and lowest at the centre of the cloud. In the case of the Ximea the relative deviation is larger than 2. In the case of the Andor the relative deviation is smaller than 0.4. For the Andor the relative difference between the estimate from the pixel density compared to the density calculated via the transmission is below 0.1, while for the Ximea the deviation is about 1. For larger cloud sizes this effect vanishes, as the mean density and pixel centre density get closer.

For the density profile beyond the cloud wings, we see larger errors again. The relative error in the transmission average settles at one. This is due to numerical errors introduced by applying an exponential and logarithm in sequence, which maps a low optical density to zero. This in turn then yields a relative error of one with respect to the pixel centre density. The relative error for the average density method is larger still and not shown in the plot. The error is introduced due to division by very low densities and numerical errors leading to comparatively large differences of the pixel centre and average density. This does not, however, concern us. When we perform the simulation, as the density enters only through the Beer-Lambert law, the low densities are mapped to a unity transmission, independent of whether we average or not.

In the simulation we decided to implement the corrections in the intensity average by averaging the density across each pixel. A numerical integration of the density across each pixel is prohibitively expensive. Instead, we opted to calculate the average mean by sampling the density of the pixel on a $n \times m$ sub-grid. We chose 20×20 for the Andor camera and 40×40 for the Ximea.

The above results also suggest adapting the fit function to actually fit the average density. Due to the required sub-sampling this increases the computational cost quite significantly. Furthermore, for cloud sizes similar or larger than the clouds discussed in this section, the deviation becomes is not significant.

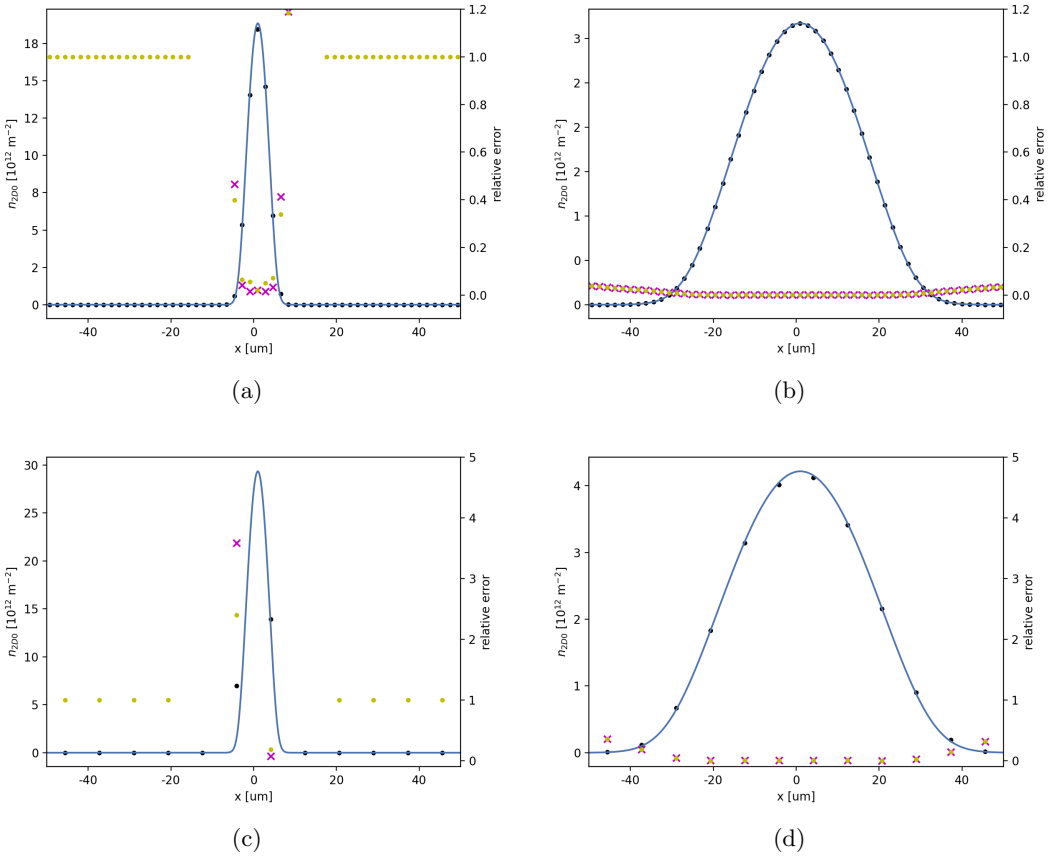

Figure 28: Comparison of average pixel density (•) and density at the pixel center. Density profiles for the Andor (top) and Ximea (bottom) for in-situ (left) and TOF (right). Relative deviations of the pixel average (×) and transmission average (●).

Appendix D Light Intensity Adjustment

The intensity as calculated for the Ximea turned out to be lower than expected (cf. 3). To understand this issue the same intensity setting of the imaging laser was measured independently by the Ximea, the Andor, a power meter and a photo-diode. In Figure 29 the results of this measurement are shown for a pulse length of $7\,\mu$s and $3\,\mu$s. The intensity was calculated from the digital counts of the camera as described in 3. For the Andor the total power was then calculated as the sum over the power incident on each pixel. For the Ximea instead of summing a Gaussian beam profile was fitted to the division image, from which the total incident power was deduced. The measurement shows that the Ximea significantly underestimates the intensity compared to the power meter and photo-diode which agree on the intensity value. The Andor appears to slightly overestimate the power. Assuming a negligible error in the effective pixel size, pulse length and quantum efficiency this implies that the sensitivity factor is underestimated for the Ximea and slightly overestimated for the Andor.

To adjust the simulation this would require to adjust the sensitivity according to the following equation:

$$\frac{I_{\text{actual}}}{I_{\text{camera}}} = \frac{s_{\text{actual}}}{s_{\text{data-sheet}}} \tag{81}$$

The ratios of the intensity as measured by the photo-diode and the intensity by the camera are

$$\begin{aligned} \text{Ximea:} \quad & I_{\text{PD}}/I_{\text{Ximea}} = 4.363 \\ \text{Andor:} \quad & I_{\text{PD}}/I_{\text{Andor}} = 0.744 \end{aligned}$$

For the simulation discussed in 6.3 the intensity and sensitivity were adjusted by these values.

Appendix E Results Data

In this appendix we will provide the fit parameters n_{2D0}, T/T_{F}, R_x R_y in the case of single time instance sweeps and T, N, T/T_{F}, T_F, $R_x(t=0)$ $R_y(t=0)$ in the case of time-of-flight sweeps.

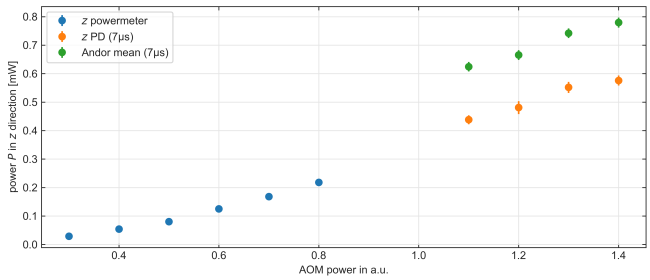

(a)

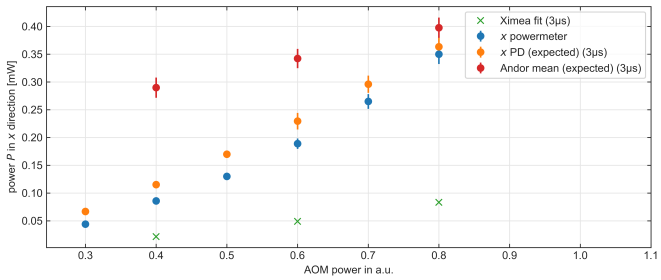

(b)

Figure 29: Power measurements of the imaging laser in (a) x-direction for $t_{\text{pulse}} = 3\,\mu$s and (b) z-direction $t_{\text{pulse}} = 7\,\mu$s. The imaging laser light in the x-direction was measured by the Andor camera, the Ximea camera, a power meter and a photo-diode (PD). In the z-direction the power was measured by the power meter, photo diode and Andor camera.The input power is determined by the setting of the acousto-optical modulator (AOM).

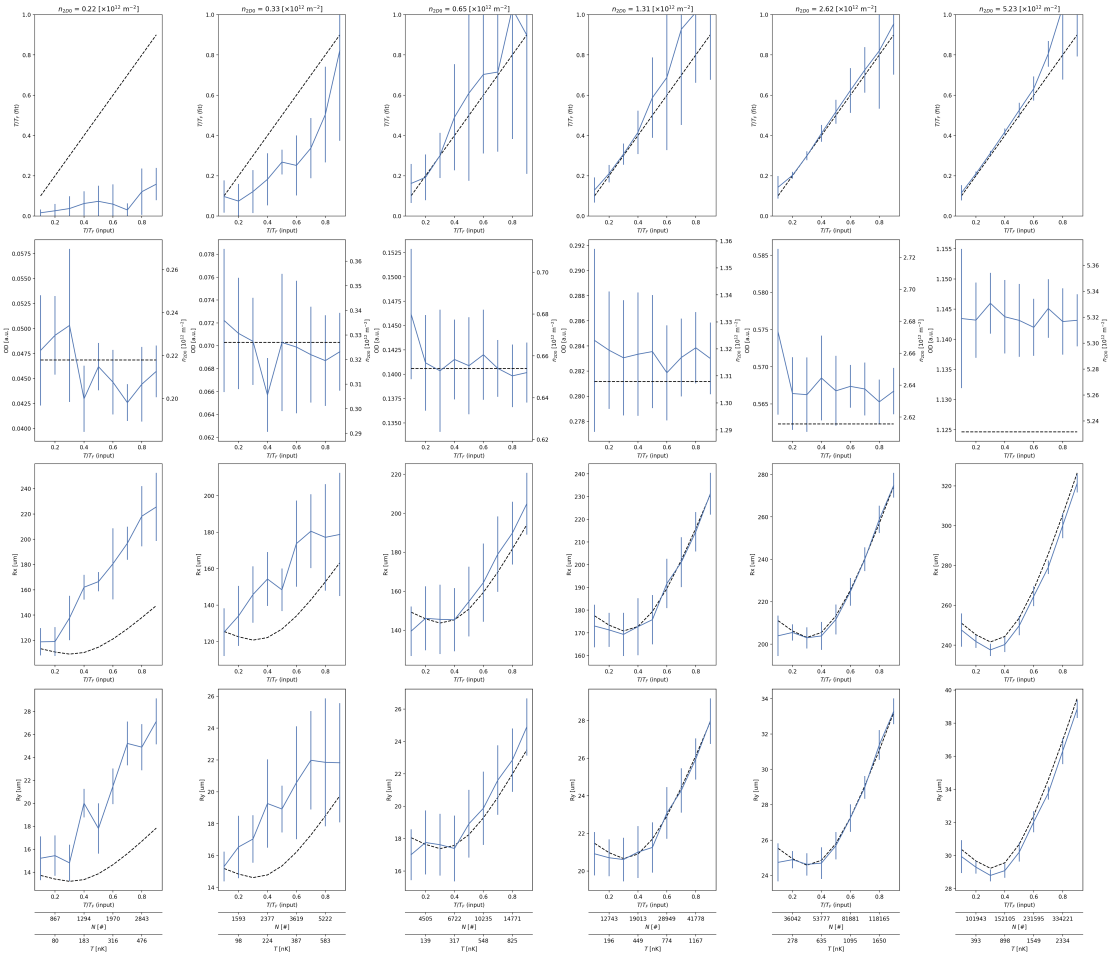

Figure 30: Fit parameter results for T/T_{F} sweep for different constant peak densities for the Andor camera. $I = 0.18 I_{\mathrm{sat}}$ (flat-field).

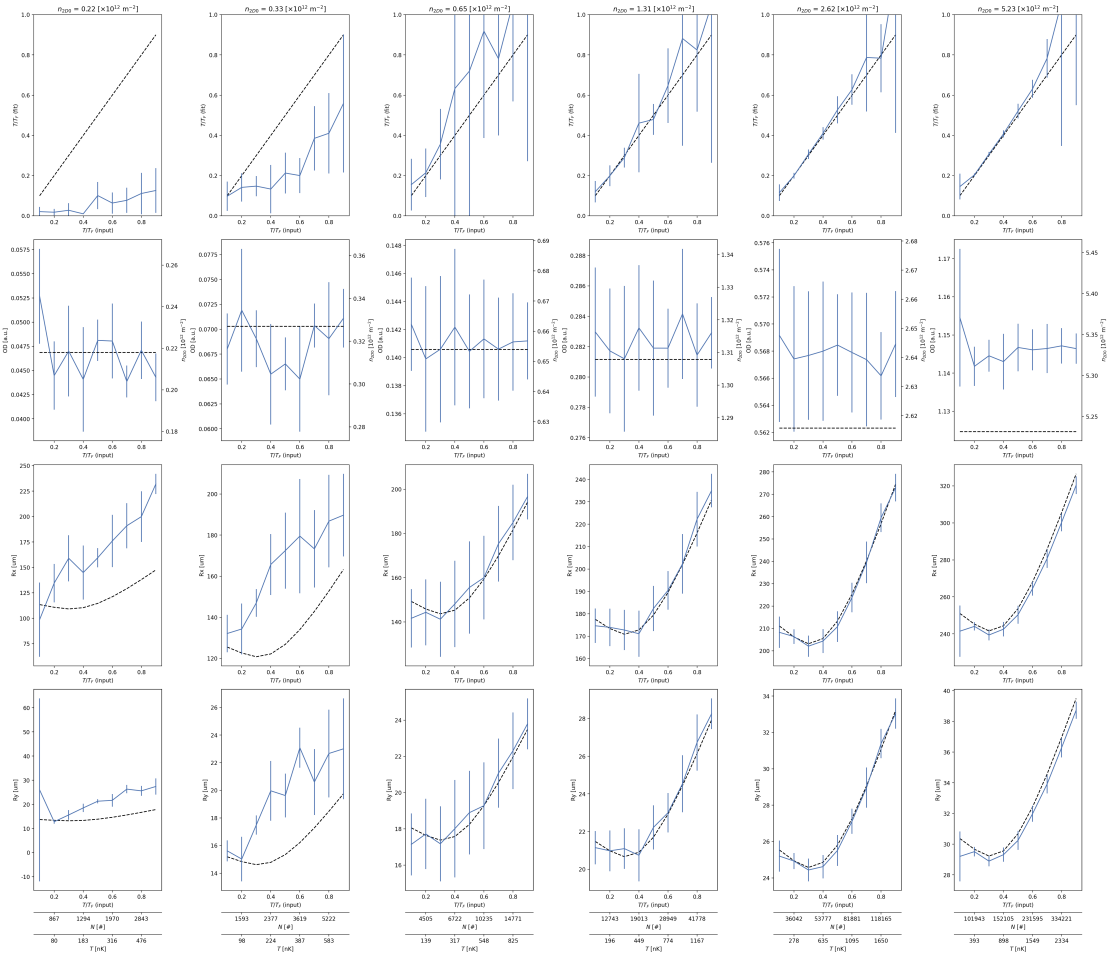

Figure 31: Fit parameter results for T/T_{F} sweep for different constant peak densities for the Andor camera. $I = 0.18 I_{\mathrm{sat}}$ (fringes).

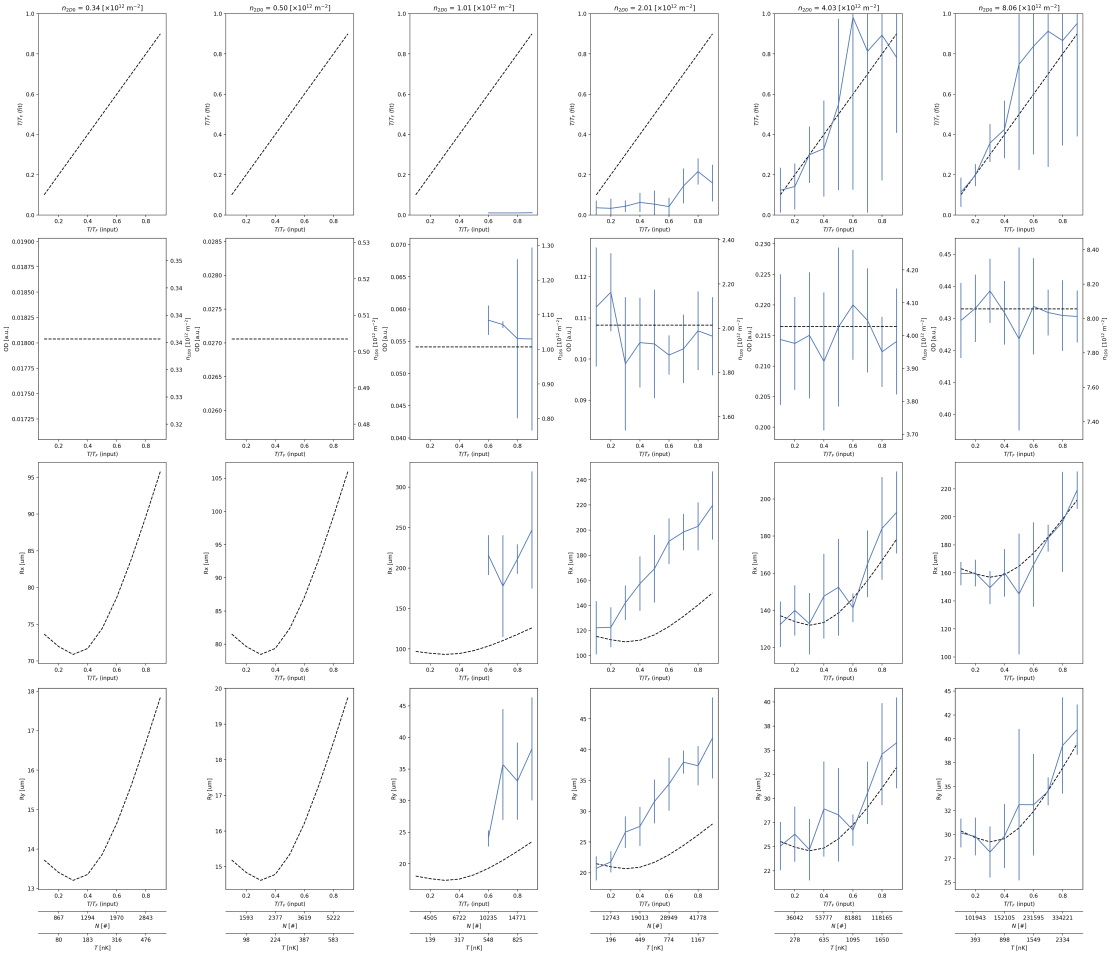

Figure 32: Fit parameter results for T/T_{F} sweep for different constant peak densities for the Andor camera. $I = 0.0049 I_{\mathrm{sat}}$ (flat-field).

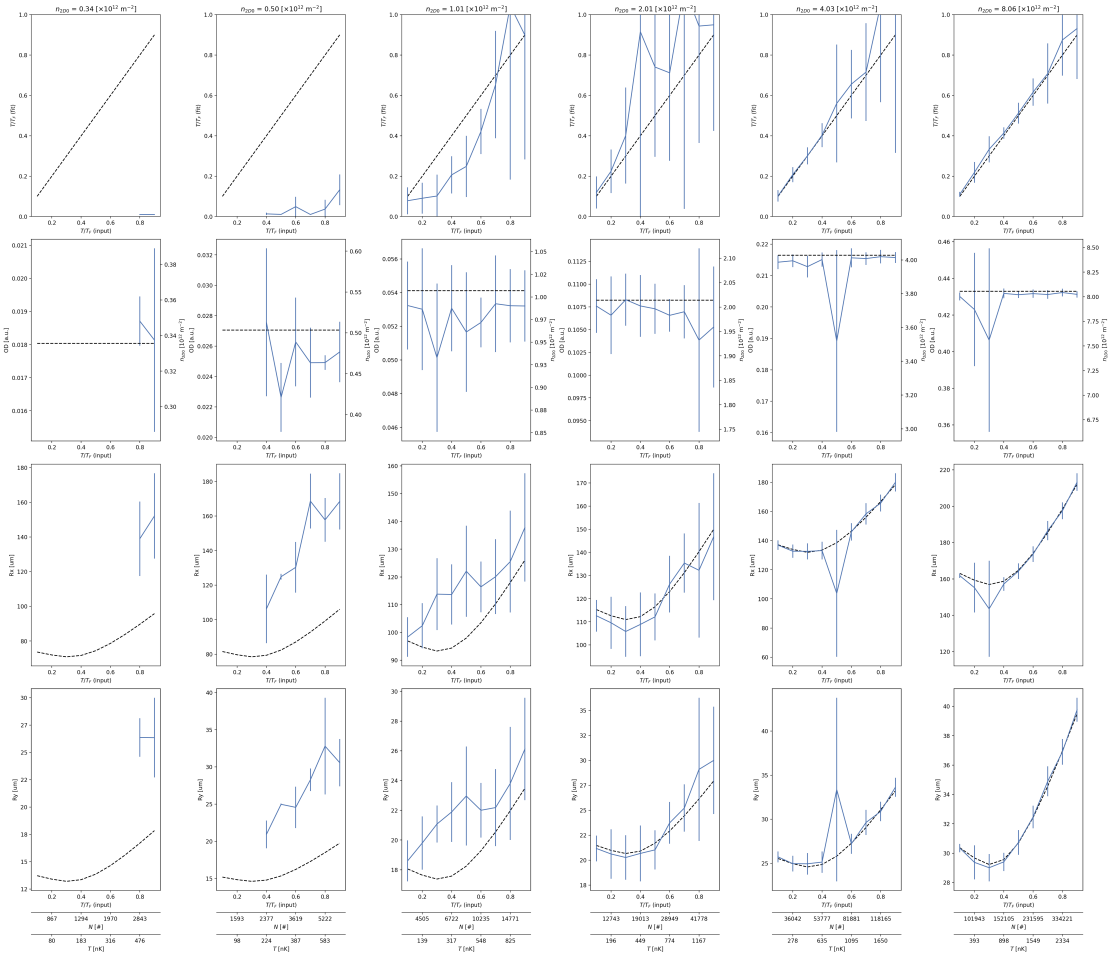

Figure 33: Fit parameter results for T/T_{F} sweep for different constant peak densities for the Andor camera. $I = 0.1 I_{\mathrm{sat}}$ (fringes).

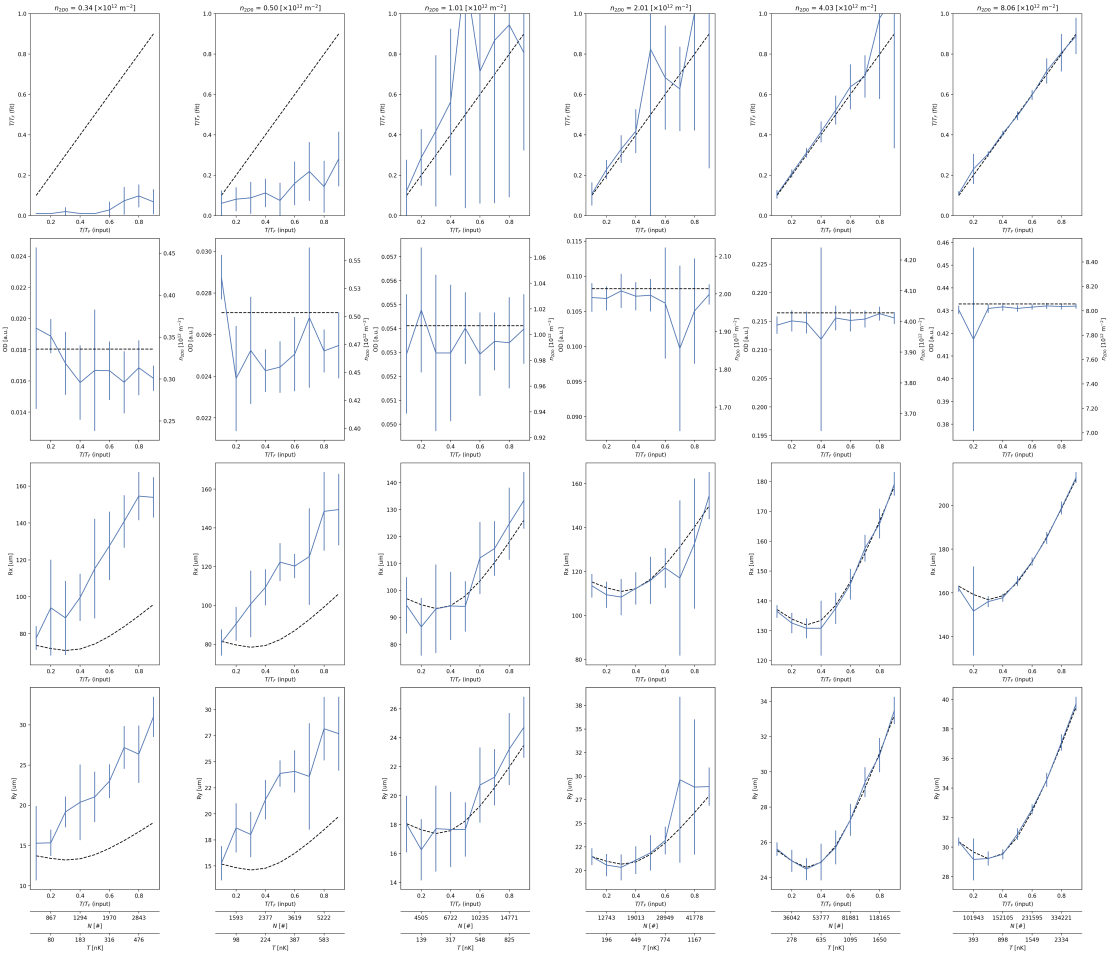

Figure 34: Fit parameter results for T/T_{F} sweep for different constant peak densities for the Andor camera. $I = 0.1 I_{\mathrm{sat}}$ (flat-field).

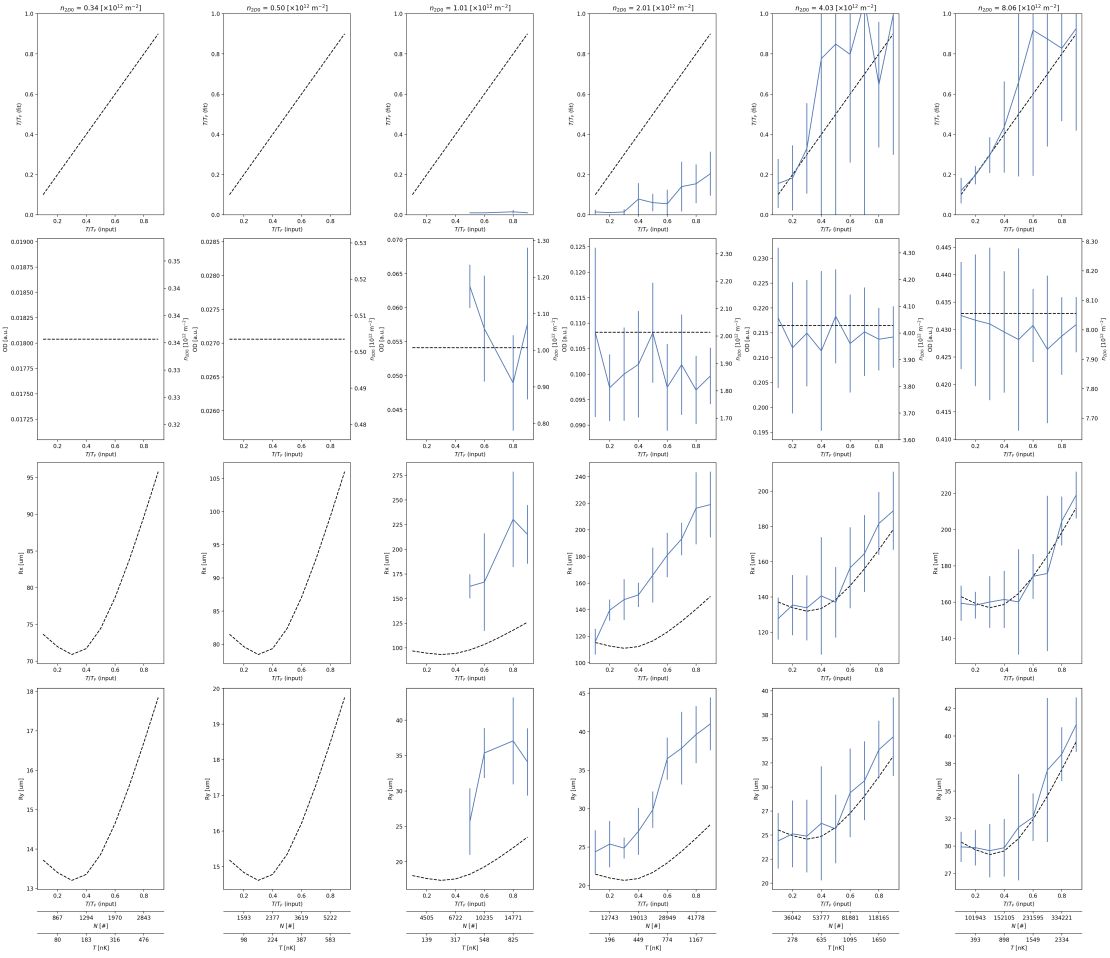

Figure 35: Fit parameter results for T/T_{F} sweep for different constant peak densities for the Andor camera. $I = 0.0049 I_{\mathrm{sat}}$ (fringes).

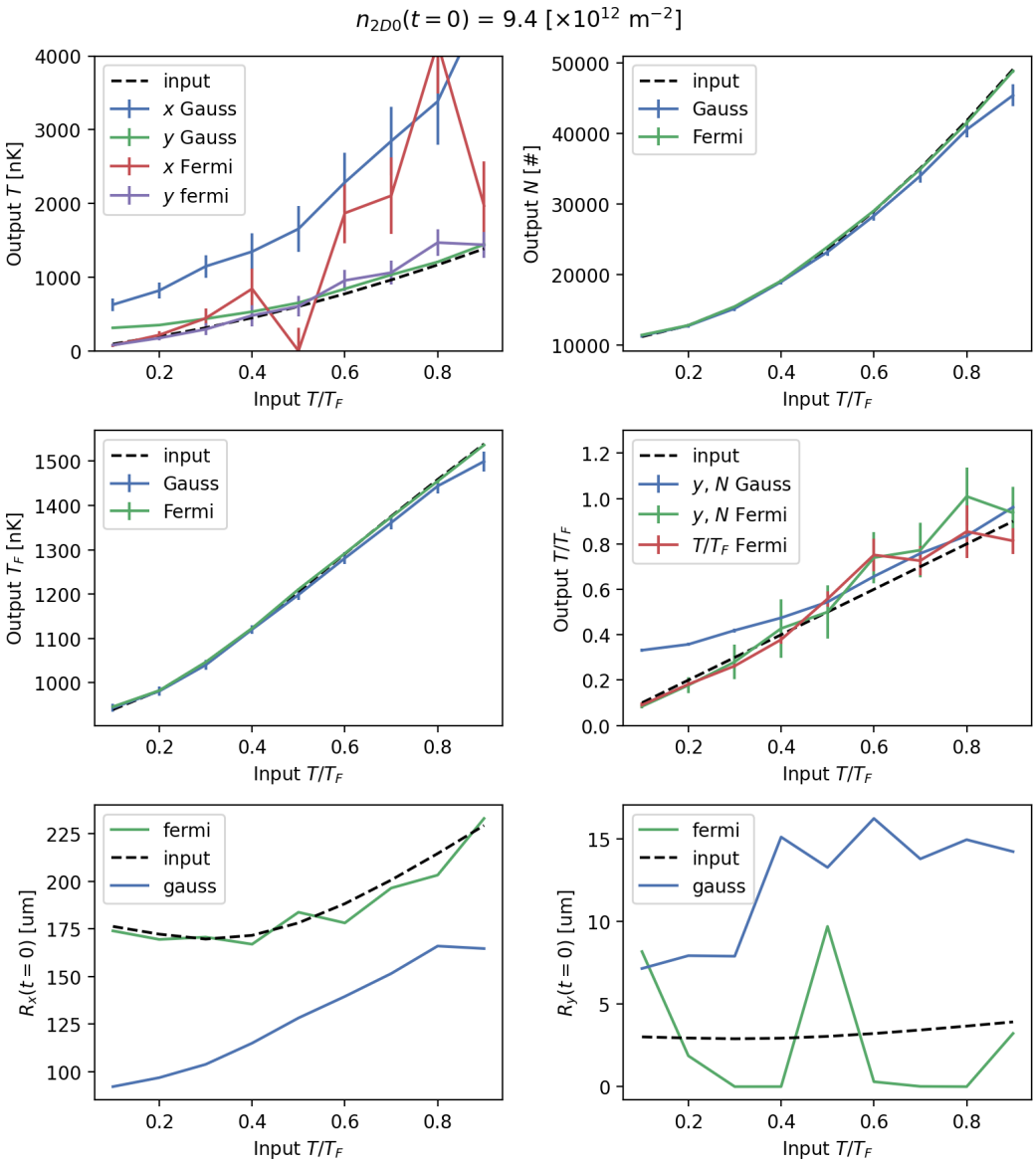

Figure 36: Fit parameter results for T/T_{F} sweep of time-of-flight simulation at $n_{2\mathrm{D}0} = 9.4 \times 10^{12}\,\mathrm{m}^{-2}$. Time series: 12 different times from 0.2 ms to 2.9 ms with 5 images each.

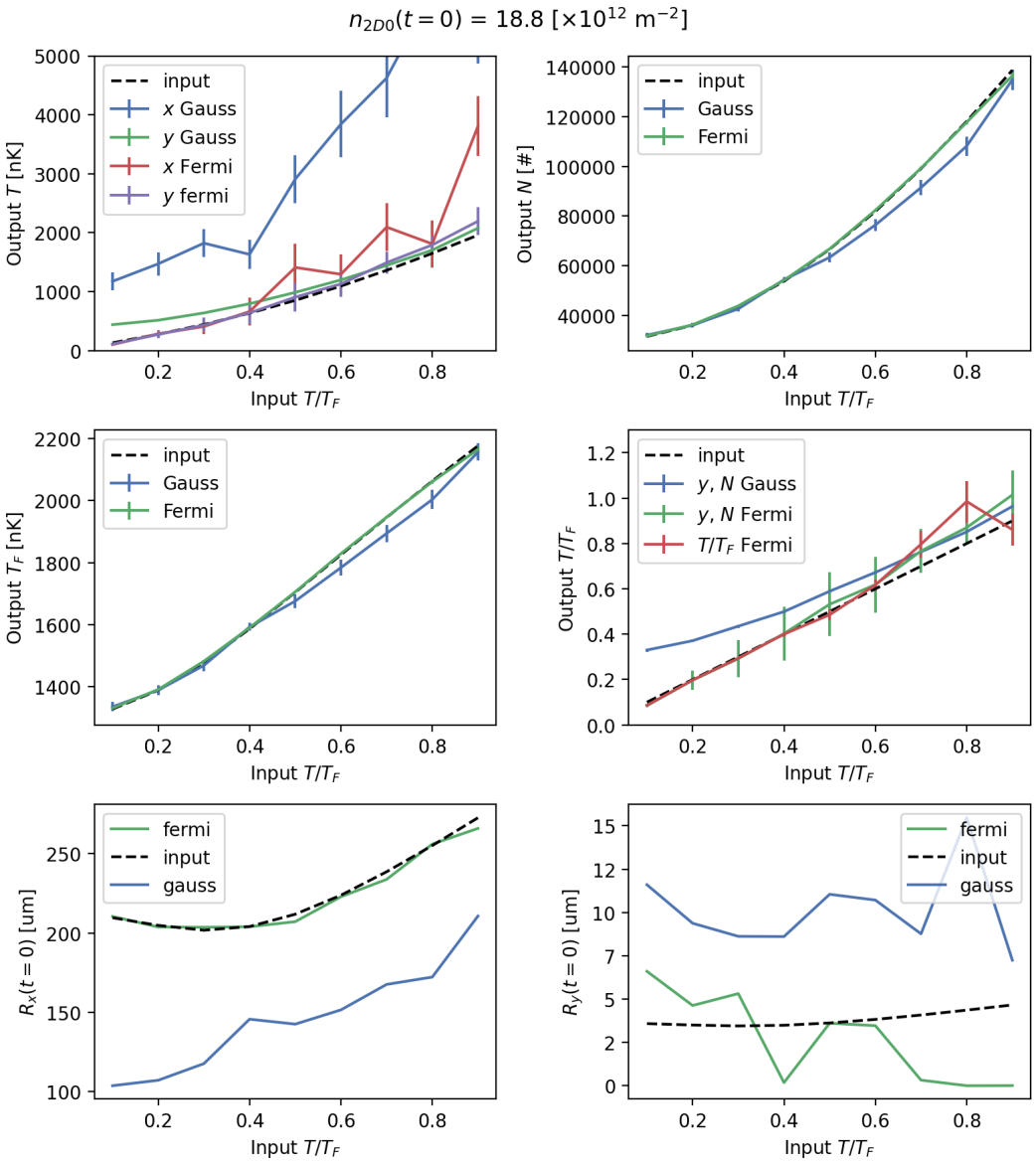

Figure 37: Fit parameter results for T/T_F sweep of time-of-flight simulation at $n_{2\mathrm{D}0} = 18.8 \times 10^{12}\,\mathrm{m}^{-2}$. Time series: 12 different times from 0.2 ms to 2.9 ms with 5 images each.

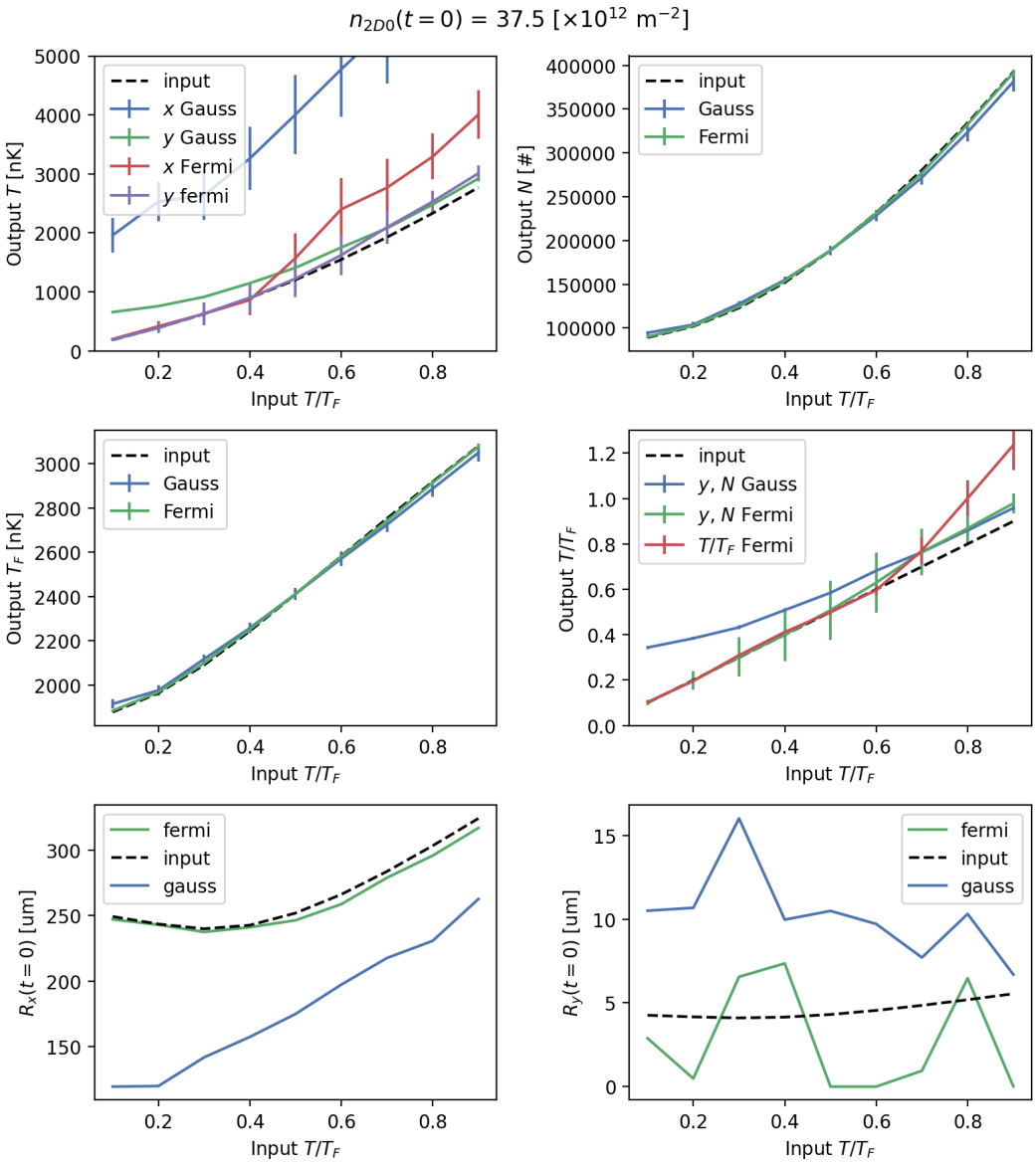

Figure 38: Fit parameter results for T/T_{F} sweep of time-of-flight simulation at $n_{2\mathrm{D}0} = 32.5 \times 10^{12}\,\mathrm{m}^{-2}$. Time series: 12 different times from 0.2 ms to 2.9 ms with 5 images each.

References

[Almudevar, 2021] Almudevar, A. (2021). *Theory of Statistical Inference*. Chapman and Hall/CRC, New York.

[Chin et al., 2010] Chin, C., Grimm, R., Julienne, P., and Tiesinga, E. (2010). Feshbach resonances in ultracold gases. *Reviews of Modern Physics*, 82 (2) pp. 1225–1286, DOI: 10.1103/RevModPhys.82.1225.

[Durini, 2014] Durini, D., editor (2014). *High Performance Silicon Imaging: Fundamentals and Applications of CMOS and CCD Sensors*. Number number 60 in Woodhead Publishing Series in Electronic and Optical Materials. Elsevier/WP, Woodhead Publishing, Amsterdam Boston Cambridge, Includes bibliographical references and index.

[Enss et al., 2020] Enss, T., Tran, B., Rautenberg, M., Gerken, M., Lippi, E., Drescher, M., Zhu, B., Weidemüller, M., and Salmhofer, M. (2020). Scattering of two heavy Fermi polarons: Resonances and quasibound states. *Physical Review A*, 102 (6) pp. 063321, DOI: 10.1103/PhysRevA.102.063321.

[Filzinger, 2018] Filzinger, M. (2018). Improved manipulation and detection of an ultracold 6 Li-133Cs mixture towards the investigation of the bose polaron. Master's thesis, Department of Physics and Astronomy, University of Heidelberg.

[Foot, 2005] Foot, C. J. (2005). *Atomic Physics*. Number 7. Atomic, Optical, and laser physics in Oxford Master Series in Physics. Oxford University Press, Oxford ; New York.

[Freund, 2022] Freund, R. (2022). Implementation of a movable optical microtrap for mixing ultracold 6Li and 133Cs towards studying the polaron scenario. Master's thesis, Department of Physics and Astronomy, University of Heidelberg, Heidelberg.

[Gehm, 2003] Gehm, M. E. (2003). Properties of 6Li.

[Heck, 2012] Heck, R. (2012). All-Optical Formation of an Ultracold Gas of Fermionic Lithium Close to Quantum Degeneracy. Master's thesis, Department of Physics and Astronomy, University of Heidelberg, Heidelberg.

[Hu, 2010] Hu, C. (2010). *Modern Semiconductor Devices for Integrated Circuits*. Prentice Hall.

[Hu and Liu, 2022] Hu, H. and Liu, X.-J. (2022). Fermi polarons at finite temperature: Spectral function and rf spectroscopy. *Physical Review A*, 105 (4) pp. 043303, DOI: 10.1103/PhysRevA.105.043303.

[Ketterle and Zwierlein, 2008] Ketterle, W. and Zwierlein, M. W. (2008). Making, probing and understanding ultracold Fermi gases. *La Rivista del Nuovo Cimento*, 31 (506) pp. 247–422, DOI: 10.1393/ncr/i2008-10033-1.

[Kong et al., 2021] Kong, Q., Siauw, T., and Bayen, A. M. (2021). *Python Programming and Numerical Methods: A Guide for Engineers and Scientists*. Elsevier, Academic Press, London.

[Konnik and Welsh, 2014] Konnik, M. and Welsh, J. (2014). High-level numerical simulations of noise in CCD and CMOS photosensors: Review and tutorial.

[Massignan et al., 2014] Massignan, P., Zaccanti, M., and Bruun, G. M. (2014). Polarons, dressed molecules and itinerant ferromagnetism in ultracold Fermi gases. *Reports on Progress in Physics*, 77 (3) pp. 034401, DOI: 10.1088/0034-4885/77/3/034401.

[Pedregosa et al., 2011] Pedregosa, F., Varoquaux, G., Gramfort, A., Michel, V., Thirion, B., Grisel, O., Blondel, M., Prettenhofer, P., Weiss, R., Dubourg, V., Vanderplas, J., Passos, A., Cournapeau, D., Brucher, M., Perrot, M., and Duchesnay, E. (2011). Scikit-learn: Machine learning in Python. *Journal of Machine Learning Research*, 12 pp. 2825–2830.

[Ratkata et al., 2021] Ratkata, A., Gregory, P. D., Innes, A. D., Matthies, A. J., McArd, L. A., Mortlock, J. M., Safronova, M. S., Bromley, S. L., and Cornish, S. L. (2021). Measurement of the tune-out wavelength for Cs 133 at 880 nm. *Physical Review A*, 104 (5) pp. 052813, DOI: 10.1103/PhysRevA.104.052813.

[Saleh and Teich, 2013] Saleh, B. E. A. and Teich, M. C. (2013). *Fundamentals of Photonics*. John Wiley & Sons, Incorporated, Somerset, UNITED STATES.

[Scazza et al., 2022] Scazza, F., Zaccanti, M., Massignan, P., Parish, M. M., and Levinsen, J. (2022). Repulsive Fermi and Bose Polarons in Quantum Gases. *Atoms*, 10 (2) pp. 55, DOI: 10.3390/atoms10020055.

[Schirotzek et al., 2009] Schirotzek, A., Wu, C.-H., Sommer, A., and Zwierlein, M. W. (2009). Observation of Fermi Polarons in a Tunable Fermi Liquid of Ultracold Atoms. *Physical Review Letters*, 102 (23) pp. 230402, DOI: 10.1103/PhysRevLett.102.230402.

[Schmidt et al., 2018] Schmidt, R., Knap, M., Ivanov, D. A., You, J.-S., Cetina, M., and Demler, E. (2018). Universal many-body response of heavy impurities coupled to a Fermi sea: A review of recent progress. *Reports on Progress in Physics*, 81 (2) pp. 024401, DOI: 10.1088/1361-6633/aa9593.

[Segal et al., 2010] Segal, S. R., Diot, Q., Cornell, E. A., Zozulya, A. A., and Anderson, D. Z. (2010). Revealing buried information: Statistical processing techniques for ultracold-gas image analysis. *Physical Review A*, 81 (5) pp. 053601, DOI: 10.1103/PhysRevA.81.053601.

[Tran et al., 2021] Tran, B., Rautenberg, M., Gerken, M., Lippi, E., Zhu, B., Ulmanis, J., Drescher, M., Salmhofer, M., Enss, T., and Weidemüller, M. (2021). Fermions Meet Two Bosons—the Heteronuclear Efimov Effect Revisited. *Brazilian Journal of Physics*, 51 (2) pp. 316–322, DOI: 10.1007/s13538-020-00811-5.

[Welz, 2024] Welz, K. (2024). Optical Trapping of Lithium-6 and Cesium-133 towards studying the Polaron Scenario [Unpublished manuscript]. Master's thesis, Department of Physics and Astronomy, University of Heidelberg, Heidelberg.

Acknowledgements

The time dedicated to working on and writing this thesis have been both challenging and rewarding. I wish to convey my gratitude to all the individuals who have supported me throughout these past months.

First and foremost, I extend my sincere appreciation to Prof. Dr. Lauriane Chomaz for granting me the opportunity to undertake this thesis under her supervision. Her mentorship and advice throughout this journey have been instrumental to its success. Her keen interest in the content of this thesis has been truly motivating.

I am particularly indebted to Tobias Krom for closely supervising this thesis, and his patience in discussing the manifold details essential to the project's success. The knowledge I have gained from him during this time is invaluable.

Furthermore, I express my sincere thanks to Eleonora Lippi, Kilian Welz and Michael Rautenberg, with whom it was a pleasure to collaborate. Their suggestions and fruitful discussions have significantly enriched this work. For all the people I had the great fortune to work with, I remain deeply impressed by their perseverance and dedication to the Mixtures experiment. I wish them all the best of luck in their pursuit of the polaron.

Last but not least, I want to thank my friends and family without whom the time spent writing this thesis would have been far less enjoyable and without whose support concluding this thesis would have been enormously more difficult. Among those dearest I want to appreciate in no particular order Lasse Köhnlein, Paul Wolf and Florian Max, who have provided generous friendship, invaluable advice and enthusiasm throughout the pursuit of this degree.

Statement of Authorship

I herewith declare that this thesis was solely composed by myself and that it constitutes my own work unless otherwise acknowledged in the text. I confirm that any quotes, arguments or concepts developed by another author and all sources of information are referenced throughout the thesis. This work has not been accepted in any previous application for a degree.

Heidelberg, July 20, 2023

Felix Borchers